2006

From galaxy-galaxy lensing to cosmological parameters

J Yoo

JL Tinker

DH Weinberg

Z Zheng

N Katz
University of Massachusetts - Amherst

See next page for additional authors

Recommended Citation

Yoo, J; Tinker, JL; Weinberg, DH; Zheng, Z; Katz, N; and Dave, R, "From galaxy-galaxy lensing to cosmological parameters" (2006). *ASTROPHYSICAL JOURNAL*. 316.
10.1086/507591

Authors

J Yoo, JL Tinker, DH Weinberg, Z Zheng, N Katz, and R Dave

FROM GALAXY-GALAXY LENSING TO COSMOLOGICAL PARAMETERS

JAIYUL YOO[1], JEREMY L. TINKER[2], DAVID H. WEINBERG[1], ZHENG ZHENG[3,4], NEAL KATZ[5],
AND ROMEEL DAVÉ[6]

accepted for publication in The Astrophysical Journal

ABSTRACT

Galaxy-galaxy lensing uses the weak distortion of background sources to measure the mean excess surface density profile, $\Delta\Sigma(r)$, around a sample of foreground lensing galaxies. We develop a method for combining $\Delta\Sigma(r)$ with the galaxy-galaxy correlation function $\xi_{\mathrm{gg}}(r)$ to constrain the matter density parameter Ω_m and the matter fluctuation amplitude σ_8, going beyond the widely used linear biasing model to reach the level of accuracy demanded by current and future measurements. We adopt the halo occupation distribution (HOD) framework, and we test its applicability to this problem by examining the effects of replacing satellite galaxies in the halos of a smoothed particle hydrodynamics (SPH) simulation with randomly selected dark matter particles from the same halos. The difference between dark matter and satellite galaxy radial profiles has a $\sim 10\%$ effect on $\Delta\Sigma(r)$ at $r < 1\ h^{-1}\mathrm{Mpc}$. However, if radial profiles are matched, then the remaining impact of individual sub-halos around satellite galaxies and environmental dependence of the HOD at fixed halo mass is $\lesssim 5\%$ in $\Delta\Sigma(r)$ for $0.1 < r < 15\ h^{-1}\mathrm{Mpc}$. We develop an analytic approximation to $\Delta\Sigma(r)$ for a specified cosmological model and galaxy HOD, improving on previous work with more accurate treatments of halo bias and halo exclusion. Tests against a suite of populated N-body simulations show that the analytic approximation is accurate to a few percent or better over the range $0.1 < r < 20\ h^{-1}\mathrm{Mpc}$. We use the analytic model to investigate the dependence of $\Delta\Sigma(r)$ and the galaxy-matter correlation function $\xi_{\mathrm{gm}}(r)$ on Ω_m and σ_8, once HOD parameters for a given cosmological model are pinned down by matching $\xi_{\mathrm{gg}}(r)$. The linear bias prediction that $\xi_{\mathrm{gm}}(r)/\xi_{\mathrm{gg}}(r) = $ constant is accurate for $r \gtrsim 2\ h^{-1}\mathrm{Mpc}$, but it fails at the $30-50\%$ level on smaller scales. The scaling of $\Delta\Sigma(r)$ with cosmological parameters, which we model as $\Delta\Sigma(r) \propto \Omega_m^{\alpha(r)}\sigma_8^{\beta(r)}$, approaches the linear bias expectation $\alpha = \beta = 1$ at $r \gtrsim 10\ h^{-1}\mathrm{Mpc}$, but α and β vary from 0.8 to 1.6 at smaller r. We calculate a fiducial $\Delta\Sigma(r)$ and scaling indices $\alpha(r)$ and $\beta(r)$ for galaxy samples that match the observed number density and projected correlation function of Sloan Digital Sky Survey galaxies with $M_r \leq -20$ and $M_r \leq -21$. Galaxy-galaxy lensing measurements for these samples can be combined with our predictions to constrain Ω_m and σ_8, taking full advantage of the high measurement precision on small and intermediate scales.

Subject headings: cosmology: theory — dark matter — galaxies: halos — gravitational lensing — large-scale structure of universe

1. INTRODUCTION

In the current paradigm of structure formation, galaxies form by the dissipative collapse of baryons in halos of cold dark matter (CDM). Understanding the relation between the galaxy and dark matter distributions is the key challenge in interpreting the observed clustering of galaxies. Large area imaging surveys have provided a new tool for untangling this relationship, galaxy-galaxy weak lensing, which uses the subtle distortion of background galaxy shapes to measure average mass profiles around samples of foreground galaxies. The last few years have seen rapid growth in this field, with the first tentative detections (Brainerd et al. 1996) giving way to high signal-to-noise ratio measurements over a substantial dynamic range (e.g., Fischer et al. 2000; McKay et al. 2001; Hoekstra et al. 2002; Sheldon et al. 2004; Mandelbaum et al.

2006).

In a cosmological context, the strength of the galaxy-galaxy lensing signal for a given galaxy sample should depend mainly on the mean matter density Ω_m and the amplitude of dark matter fluctuations σ_8, since increasing either parameter enhances the average amount of dark matter around galaxies and thereby amplifies the lensing signal.[7] In this paper, we develop tools for constraining Ω_m and σ_8 with galaxy-galaxy lensing and galaxy clustering measurements, using halo occupation models of galaxy bias that are applicable from the linear regime into the fully non-linear regime. Our approach extends and complements earlier work by Seljak (2000), Guzik & Seljak (2001, 2002), Tasitsiomi et al. (2004), and Mandelbaum et al. (2005).

Galaxy-galaxy lensing measures the profiles of mean tangential shear around galaxies. With knowledge of source and lens redshift distributions, this tangential shear can be converted to excess surface density,

$$\Delta\Sigma(r) \equiv \bar{\Sigma}(<r) - \bar{\Sigma}(r), \qquad (1)$$

where $\bar{\Sigma}(<r)$ is the mean surface density interior to the disk of projected radius r and $\bar{\Sigma}(r)$ is the averaged surface density in a thin annulus of the same radius (Miralda-Escudé 1991a;

[1] Department of Astronomy, The Ohio State University, 140 West 18th Avenue, Columbus, OH 43210; jaiyul@astronomy.ohio-state.edu, dhw@astronomy.ohio-state.edu

[2] Kavli Institute for Cosmological Physics, University of Chicago, Chicago, IL 60637; tinker@cfcp.uchicago.edu

[3] School of Natural Sciences, Institute for Advanced Study, Einstein Drive, Princeton, NJ 08540; zhengz@ias.edu

[4] Hubble Fellow

[5] Departments of Physics and Astronomy, University of Massachusetts, Amherst, MA 01003; nsk@kaka.phast.umass.edu

[6] Steward Observatory, University of Arizona, Tucson, AZ 85721; rdave@as.arizona.edu

[7] Here σ_8 is the rms linear theory matter fluctuation in spheres of radius $8\ h^{-1}\mathrm{Mpc}$, with $h \equiv H_0/100\ \mathrm{km\,s^{-1}Mpc^{-1}}$.

Sheldon et al. 2004).[8] The excess surface density profile is itself related to the galaxy-matter cross-correlation function $\xi_{\rm gm}$ by

$$\Delta\Sigma(r) = \rho_c \Omega_m \times \tag{2}$$
$$\left[\frac{2}{r^2} \int_0^r \int_{-\infty}^{\infty} r' \xi_{\rm gm}\left(\sqrt{r'^2 + z^2}\right) \, dz \, dr' - \int_{-\infty}^{\infty} \xi_{\rm gm}(r,z) dz \right],$$

where ρ_c is the critical density of the universe. Johnston et al. (2005) discuss and test methods of inverting $\Delta\Sigma(r)$ to obtain the three-dimensional $\xi_{\rm gm}(r)$. Here we treat $\Delta\Sigma(r)$ as the primary observable and concentrate on predicting it directly.

On large scales, where matter fluctuations are linear, the relation between the matter auto-correlation function $\xi_{\rm mm}$, the galaxy-matter cross-correlation function $\xi_{\rm gm}$, and the galaxy auto-correlation function $\xi_{\rm gg}$ may be adequately described by the linear bias model,

$$\xi_{\rm gg} = b^2 \xi_{\rm mm}, \tag{3}$$

$$\xi_{\rm gm} = b \xi_{\rm mm}, \tag{4}$$

where the linear bias factor b is the same in both equations (Kaiser 1984). Thus, measurements of $\xi_{\rm gg}$ and $\Delta\Sigma \propto \xi_{\rm gm}\Omega_m$ can be combined to yield Ω_m/b. Since the amplitude of galaxy fluctuations is $\sigma_{8,\rm g} = b\sigma_8$ in the linear bias model, this method in turn constrains the product $\sigma_8\Omega_m$. Redshift-space distortions of the galaxy power spectrum and the abundance of rich galaxy clusters as a function of mass both depend on a parameter combination that is approximately $\sigma_8\Omega_m^{0.6}$ (Kaiser 1987; White et al. 1993), so the combination of galaxy-galaxy lensing with either of these measurements can break the degeneracy between σ_8 and Ω_m. However, the linear bias approximation may break down on the scales $r \lesssim$ several $h^{-1}{\rm Mpc}$ where $\Delta\Sigma(r)$ is measured with high precision. Moreover, if the relation between galaxy and matter density contrasts is linear but stochastic, then the linear bias factor b in equation (4) should be replaced by $br_{\rm gm}$, where $r_{\rm gm}$ is the galaxy-matter cross-correlation coefficient (Pen 1998; Dekel & Lahav 1999), and the constrained combination becomes $\sigma_8\Omega_m r_{\rm gm}$ even in the linear regime. The addition of $r_{\rm gm}$ as a free parameter reduces the cosmological constraining power of the $\Delta\Sigma$ and $\xi_{\rm gg}$ combination, and restoring it requires an independent determination of $\xi_{\rm mm}$. Cosmic shear measurements can provide such a determination (Blandford et al. 1991; Miralda-Escudé 1991b; Kaiser 1992), but these measurements are challenging and suffer larger systematic errors than galaxy-galaxy lensing.

Hoekstra et al. (2001, 2002) used imaging and photometric redshift data from the Red-Sequence Cluster Survey (Gladders & Yee 2001) to measure aperture fluctuations proportional to $\xi_{\rm gg}$, $\xi_{\rm gm}$, and $\xi_{\rm mm}$. They provided tentative evidence that b and r are each individually scale-dependent but that the ratio $b/r_{\rm gm}$ is approximately constant, with $b/r_{\rm gm} \simeq 1$ for $\Omega_m = 0.3$. Using the Sloan Digital Sky Survey (SDSS, York et al. 2000), which provides spectroscopic redshifts of lens galaxies and image shapes and photometric redshifts of source galaxies, Sheldon et al. (2004) detected galaxy-galaxy lensing and measured the galaxy-matter correlation function from 0.025 to 10 $h^{-1}{\rm Mpc}$ (see Fischer et al. 2000 and McKay et al. 2001 for earlier SDSS measurements, and Mandelbaum et al. 2006 for more recent measurements at $r \leq 2$ $h^{-1}{\rm Mpc}$). They found that the galaxy-galaxy correlation function and the galaxy-matter correlation function

agree in shape, with an amplitude ratio that implies $b/r_{\rm gm} = (1.3 \pm 0.2)(\Omega_m/0.27)$ for galaxy samples of mean luminosity $\langle L \rangle \sim L_\star$.

To circumvent the limitations of the linear bias approximation, we model galaxy-galaxy and galaxy-matter correlations using halo occupation methods, following the lead of Seljak (2000), Berlind & Weinberg (2002), and Guzik & Seljak (2002). The halo occupation distribution (HOD) provides a fully non-linear description of the relation between galaxies and mass by specifying the probability $P(N|M)$ that a halo of virial mass M contains N galaxies of a particular class, along with any spatial or velocity biases within individual halos.[9] Numerous authors have used this approach to compute analytic approximations for galaxy and dark matter clustering statistics (e.g., Ma & Fry 2000; Seljak 2000; Scoccimarro et al. 2001; Seljak 2001; Sheth et al. 2001a; White 2001; see review by Cooray & Sheth 2002), and to model observed galaxy clustering (e.g., Jing et al. 1998, 2002; Peacock & Smith 2000; Kochanek & White 2001; Bullock et al. 2002; Magliocchetti & Porciani 2003; Yang et al. 2003; Porciani et al. 2004; Zehavi et al. 2004, 2005a; Zheng 2004; Abazajian et al. 2005; Collister & Lahav 2005; Lee et al. 2006; Tinker et al. 2006). Theoretical predictions for the HOD of different galaxy types have been calculated using semi-analytic models, hydrodynamic simulations, and high resolution N-body calculations that identify "galaxies" with dark matter substructures (Kauffmann et al. 1997; Benson et al. 2000; White et al. 2001; Yoshikawa et al. 2001; Berlind et al. 2003; Kravtsov et al. 2004; Zentner et al. 2005; Zheng et al. 2005).

Our basic approach to modeling galaxy-galaxy lensing in the HOD framework is similar to that adopted by Tinker et al. (2005, 2006) for modeling mass-to-light ratios and redshift-space distortions. Since measurements of the galaxy power spectrum, cosmic microwave background anisotropies, and the Lyα forest yield tight constraints on the shape of the linear matter power spectrum $P_{\rm lin}(k)$ (see, e.g., Spergel et al. 2003; Tegmark et al. 2004; Cole et al. 2005; Seljak et al. 2005), we take this shape to be fixed and investigate the parameter space spanned by Ω_m and σ_8. For a given choice of Ω_m and σ_8, we first choose HOD parameters to match observations of the projected galaxy correlation function $w_p(r_p)$ (see, e.g., Zehavi et al. 2004, 2005a). We then predict the excess surface density profile $\Delta\Sigma(r)$ for this combination of Ω_m, σ_8, and HOD. Comparison to galaxy-galaxy lensing measurements then determines the acceptable combinations of Ω_m and σ_8. We impose the observed galaxy-galaxy correlation function as a constraint on the HOD, instead of taking ratios as in the linear bias analysis. There is no need for an unknown cross-correlation coefficient $r_{\rm gm}$ because any "stochasticity" between galaxy and mass density fields is automatically incorporated in the HOD calculation. Our strategy complements that of Guzik & Seljak (2001, 2002) and Mandelbaum et al. (2005), who focus on constraining halo masses, halo profiles, and satellite fractions using $\Delta\Sigma(r)$ alone, rather than constraining Ω_m and σ_8 from the combination of $\Delta\Sigma(r)$ and $\xi_{\rm gg}(r)$.

Our eventual conclusions about the cosmological constraining power of galaxy-galaxy lensing measurements rest on an analytic model for computing $\Delta\Sigma(r)$ given $P_{\rm lin}(k)$, Ω_m, σ_8,

---

[8] We interchangeably use r to refer to a projected (two-dimensional) or a three-dimensional radius.

[9] Throughout this paper, we use the term "halo" to refer to a dark matter structure of overdensity $\rho/\bar{\rho}_m \simeq 200$, in approximate dynamical equilibrium, which may contain a single bright galaxy or a group or a cluster of galaxies.

and the galaxy HOD. This model is similar in spirit to that of Guzik & Seljak (2002), but it differs in many details, in part because we define the calculational problem in different terms. We test the analytic model against numerical calculations, in which we use a specified HOD to populate the halos of N-body simulations, placing "central" galaxies at the halo potential minimum and "satellite" galaxies at the locations of randomly selected dark matter particles. Both our analytic model and our method of populating N-body halos ignore the impact of dark matter *subhalos* around the individual satellite galaxies orbiting in a larger halo. To begin, therefore, we test the validity of the "populated halo" approach itself, by comparing $\Delta\Sigma(r)$ for the galaxy population of a smoothed particle hydrodynamics (SPH) simulation to that found by populating the dark matter halos of this simulation with "galaxies" placed on randomly selected dark matter particles. This test shows that satellite subhalos have minimal impact on $\Delta\Sigma(r)$ and that the populated halo approach is acceptable for our purpose. We also show that any environmental dependence of halo galaxy content at fixed halo mass (Gao et al. 2005; Harker et al. 2006) has little discernible impact on the galaxy-galaxy or galaxy-matter correlation functions in our SPH simulations. More generally, our SPH and N-body tests indicate that the analytic model should be accurate at the $5-10\%$ level on scales $r \gtrsim 0.1~h^{-1}$Mpc. This level of accuracy is acceptable for present purposes, since the current measurement errors are typically $\gtrsim 25\%$ per radial bin (e.g., Sheldon et al. 2004), but still higher accuracy will be needed in the long term.

In our N-body and analytical calculations, we use HOD parameters for SDSS galaxy samples with absolute-magnitude limits $M_r \leq -20$ and $M_r \leq -21$ (Zehavi et al. 2005b) for purposes of illustration.[10] The results presented in § 5 therefore yield predictions of the weak lensing signal for these galaxy samples as a function of Ω_m and σ_8. The analytic model can be used to make predictions for other galaxy samples given measurements of the projected correlation function as input.

2. SPH GALAXIES VERSUS POPULATED HALOS

To test the validity of our N-body method for calculating galaxy-galaxy lensing predictions (see § 3), we first examine an SPH simulation of a ΛCDM (inflationary cold dark matter with a cosmological constant) universe. This simulation is described in detail by Weinberg et al. (2004), who, among other things, present predicted galaxy-matter correlations and compare them to recent observations. Here we want to know whether the individual dark matter subhalos retained by baryonic galaxies in groups and clusters make an important contribution to the galaxy-galaxy lensing signal.

In brief, the simulation uses Parallel TreeSPH (Hernquist & Katz 1989; Katz, Weinberg, & Hernquist 1996; Davé et al. 1997) to model a 50 h^{-1}Mpc comoving cube with 144^3 dark matter particles and 144^3 gas particles. The cosmological parameters are $\Omega_m = 0.4$, $\Omega_\Lambda = 0.6$, $h = 0.65$, $n = 0.95$, $\Omega_b h^2 = 0.02$, and $\sigma_8 = 0.80$. The gravitational forces are softened with a 10 h^{-1}kpc (comoving) spline kernel. Radiative cooling leads to the formation of dense baryonic clumps (Katz et al. 1992; Evrard et al. 1994), which form stars according to the algorithm described by Katz, Weinberg, & Hernquist (1996). Galaxies are identified by applying the SKID (Spline-Kernel Interpolated DENMAX; see Katz, Weinberg, & Hernquist 1996) algorithm

to the population of stars and cold, dense gas particles.[11] Tests with simulations of varying resolution show that the simulated galaxy population is complete above a baryonic mass (stars plus cold, dense gas) of $\sim 64~m_{\rm SPH}$, corresponding to $5.4 \times 10^{10} M_\odot$ ($3.5 \times 10^{10}~h^{-1}M_\odot$) for this simulation. The space density of galaxies above this mass threshold is $\bar{n}_g = 0.02~(h^{-1}{\rm Mpc})^{-3}$, corresponding to that of observed galaxies with $M_r \leq -18.6$ ($L > 0.18 L_\star$; Blanton et al. 2003). We use this mass-thresholded galaxy sample for the tests below.

We identify dark matter halos by applying the friends-of-friends algorithm (FOF; Davis et al. 1985) to the dark matter particle distribution, with a linking length of 0.2 times the mean interparticle separation, or 70 h^{-1}kpc. We associate each SPH galaxy with the halo containing the dark matter particle closest to its center of mass. To create "populated halo" galaxy catalogs, we replace the SPH galaxies in each halo with an equal number of artificial galaxies positioned on dark matter particles. The first "central" galaxy of each occupied halo is placed at the location of the dark matter particle with lowest potential energy (computed using only halo members). Any additional, "satellite" galaxies are placed on randomly selected dark matter particles. Satellites therefore follow the radial profile of dark matter within each halo, while any detailed association between satellites and the centers of dark matter subhalos is erased.

The left panels of Figure 1 compare the galaxy-galaxy correlation functions, galaxy-matter correlation functions, and excess surface density profiles of the SPH galaxies and the populated halo galaxy catalogs. Results for the populated halos are an average over 10 realizations of the galaxy locations, and error bars show the dispersion among the ten realizations. (Note that these do *not* represent the uncertainty on the mean, which would be a factor of three smaller, and they do not include the uncertainty owing to the finite simulation volume, since we are comparing galaxy catalogs in the same volume). The galaxy-galaxy and galaxy-matter correlations of the two catalogs are very similar at $r \gtrsim 0.5~h^{-1}$Mpc, while at smaller separations the populated halo catalog has correlations that are stronger by up to 20%. The excess surface density profile is calculated by directly counting galaxy-dark matter particle pairs in projection to compute $\bar{\Sigma}(< r)$ and $\Sigma(r)$, not by integrating the three-dimensional $\xi_{\rm gm}(r)$. We count all projected pairs through the 50 h^{-1}Mpc box and average results from the three orthogonal projections of the box; noise from uncorrelated foreground and background particles cancels out because we have many galaxy targets. Relative to the SPH galaxy catalog, $\Delta\Sigma(r)$ for the populated halo catalog starts about 10% low, rises to 10% above at $r \sim 0.5~h^{-1}$Mpc, then agrees closely beyond $r \sim 1~h^{-1}$Mpc.

The modest deviations between the SPH galaxy and populated halo results could reflect either the impact of satellite subhalos or differences between the radial profiles of SPH satellites and dark matter. To separate the two effects, we adopt a different method of populating halos that ensures identical radial profiles, by placing each satellite at the radial distance of the corresponding SPH satellite but choosing a random orientation for the radius vector. Results are shown on the right panels of Figure 1. The differences in $\xi_{\rm gg}(r)$, $\xi_{\rm gm}(r)$, and $\Delta\Sigma(r)$ are greatly reduced, demonstrating that they arise mainly from the different radial profiles of SPH

---

[10] Throughout the paper, we quote absolute magnitudes for $h = 1$; more generally, these thresholds correspond to $M_r - 5\log h$.

[11] We use the implementation of SKID by J. Stadel & T. Quinn, available at http://www-hpcc.astro.washington.edu/tools/skid.html
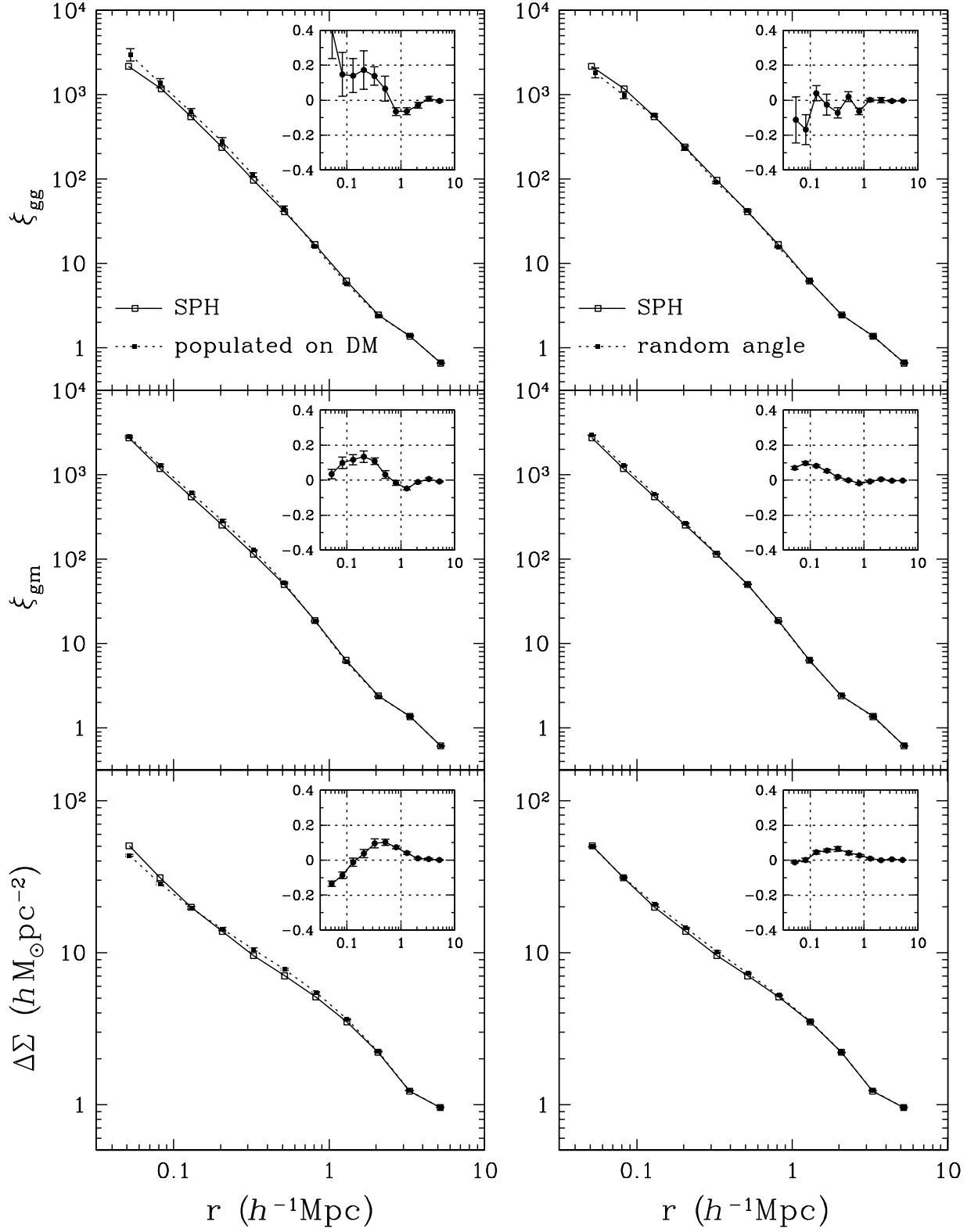
FIG. 1.— Galaxy-galaxy correlation functions (*top panels*), galaxy-matter correlation functions (*middle panels*), and $\Delta\Sigma(r)$ profiles (*bottom panels*) for the true galaxy population of an SPH simulation (*solid lines*) and the populated dark matter halos of this simulation (*dotted lines*, see text). Inset panels show the fractional difference between the SPH and populated halo results. In the left-hand panels, satellite galaxies in the populated halos are placed on randomly selected dark matter particles, while in the right-hand panels they are forced to follow the radial profile of satellite galaxies in the SPH simulation.
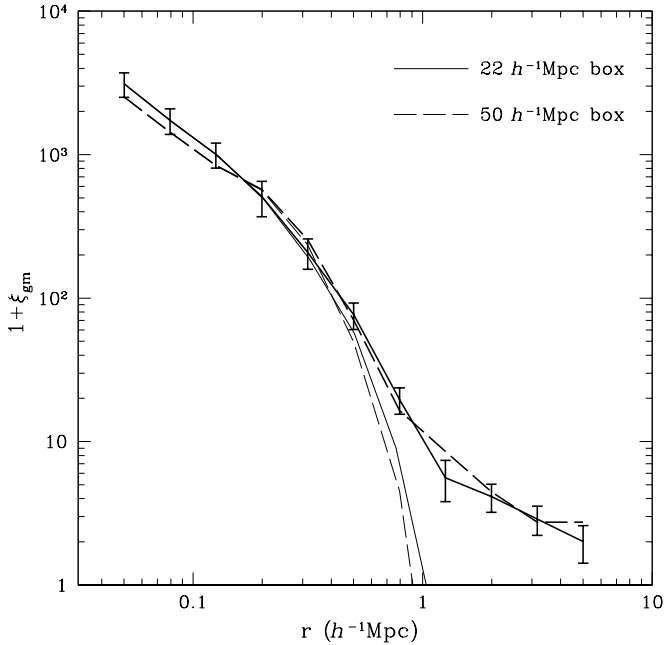
FIG. 2.— Comparison of galaxy-matter correlation functions for satellite galaxies of our standard SPH simulations (*dashed lines*), which uses 144^3 particles in a 50 h^{-1}Mpc box, to those of a higher resolution, smaller volume simulation (128^3 particles in a 22.222 h^{-1}Mpc box, *solid lines*). In both simulations we select halos in the mass range $6 \times 10^{12} h^{-1} M_\odot \lesssim M \lesssim 2 \times 10^{13} h^{-1} M_\odot$ and satellite galaxies above the 3.5×10^{10} $h^{-1} M_\odot$ resolution limit of the larger volume run. Heavy lines show the full satellite-matter cross-correlation function, while light lines include only matter in the satellite's parent halo (the one-halo term). Error bars are computed for the smaller simulation via bootstrap resampling.

satellite galaxies and dark matter; specifically, the SPH satellites are less concentrated towards the halo center than the dark matter. With matched radial profiles, the populated halos still have slightly larger $\xi_{gm}(r)$ at $r \lesssim 0.1$ h^{-1}Mpc, in part because there are usually offsets of this magnitude between the location of the SPH central galaxy and the position of the most bound dark matter particle. However, the differences in $\Delta\Sigma(r)$ are now smaller than 10% at all r.

We conclude that it is safe to ignore the subhalos of individual satellite galaxies when computing $\Delta\Sigma(r)$ for a full galaxy sample. Indeed, the remaining residuals in Figure 1, a consequence of the central galaxy offsets mentioned above, are opposite in sign to those expected from satellite subhalos. Satellites in the SPH simulation *do* reside in individual dark matter subhalos (Weinberg et al. 2006), but these are tidally truncated, and at small separations $\Delta\Sigma(r)$ is dominated by the contribution of the more numerous, central galaxies (see § 4.2 below). The small impact of satellite subhalos on $\Delta\Sigma(r)$ is therefore unsurprising, and was anticipated by earlier analytic modeling (Guzik & Seljak 2002; Mandelbaum et al. 2005).

Nonetheless, one might worry that the absence of *any* subhalo signal in Figure 1 is an artifact of our simulation's finite mass resolution, leading to an artificially high degree of tidal truncation. To test this possibility, we compare results from this simulation to those of a simulation of the same cosmological model with a factor of eight higher mass resolution but smaller volume. This simulation uses 128^3 dark matter particles and 128^3 gas particles in a volume 22.222 h^{-1}Mpc on a side. In each simulation, we select all halos in the mass

range 6×10^{12} $h^{-1} M_\odot \lesssim M \lesssim 2 \times 10^{13}$ $h^{-1} M_\odot$ and measure the galaxy-matter correlation function for *satellites* in these halos above the baryonic mass threshold of the larger volume, lower resolution simulation. The 50 h^{-1}Mpc box contains 78 halos and 188 satellite galaxies satisfying these cuts, while the 22.222 h^{-1}Mpc box contains 12 halos and 33 satellites. As shown in Figure 2, the satellite galaxy-matter correlations are equal in the two simulations to within the statistical errors, which are estimated by bootstrap resampling of the galaxies in the smaller simulation. The average mass profiles around satellites are therefore robust over a factor of eight in mass resolution.

Standard HOD calculations assume that the halo occupation function $P(N|M)$ has no direct dependence on a halo's larger scale environment. This assumption is motivated by the excursion set derivation of the Extended Press-Schechter formalism (Bond et al. 1991), which, in its simplest form, predicts that a halo's formation history is uncorrelated with its environment at fixed mass (White 1996). The correlation of galaxy properties with large scale environment emerges indirectly from the correlation with halo mass because high mass halos are more common in dense environments. Blanton et al. (2006) showed that the observed correlation of red galaxy fraction with overdensity measured at 6 h^{-1}Mpc is entirely accounted for by the correlation with overdensity measured at the 1 h^{-1}Mpc scale characteristic of individual large halos. However, while early N-body studies showed at most weak correlations between halo formation time and environment at fixed mass for halos with $M \gtrsim 10^{13} h^{-1} M_\odot$ (Lemson & Kauffmann 1999; Sheth & Tormen 2004), Gao et al. (2005) have recently shown that there is a much stronger correlation for lower mass halos, with the older halos being more strongly clustered (see also Sheth & Tormen 2002; Harker et al. 2006 discuss the potential origin of environmental correlations in the excursion set formalism). Berlind et al. (2003), examining the same SPH simulation and galaxy sample that we have used here, showed that the mean number of galaxies as a function of halo mass, $\langle N \rangle_M$, is independent of halo environment within the statistical uncertainties imposed by the finite simulation volume. However, in light of Gao et al.'s (2005) result, we have carried out an experiment to explicitly examine the possible impact of environmental dependence of $P(N|M)$ on galaxy-galaxy and galaxy-matter correlations.

In the populated halo calculations shown in Figure 1, the number of galaxies assigned to each halo is equal to the number of SPH galaxies, so any environmental dependence predicted by the SPH simulation is also built into the populated halo distribution. We eliminate the environmental dependence by shuffling the galaxy populations among halos of similar mass. Specifically, we sort the halos by mass and replace the number of galaxies N_i in the halo of rank i with the number N_{i+1} in halo $i+1$, then recalculate $\xi_{gg}(r)$, $\xi_{gm}(r)$, and $\Delta\Sigma(r)$, averaging over ten realizations of galaxy positions *within* halos. We repeat the exercise with the substitutions $N_{i+1} \to N_{i+2}$, N_{i-1}, and N_{i-2} so that we can average over four different halo shufflings and compute the statistical error on the mean. The sampling of the halo mass function is sparse for the highest mass halos in the simulation, so at high masses we cannot exchange the galaxy contents of halos without significantly changing $P(N|M)$ itself. We therefore keep the galaxy populations of the N_{fix} most massive halos fixed, with $N_{fix} = 5$ or 20. For $N_{fix} = 5$, we are shuffling the contents of all halos with $M < 9.0 \times 10^{13}$ $h^{-1} M_\odot$, and for $N_{fix} = 20$ we are shuffling the

TABLE 1
PARAMETERS OF GADGET SIMULATIONS AND HOD PARAMETERS

Model	Ω_m	σ_8	$M_{\min}(h^{-1}M_\odot)$	$M_1(h^{-1}M_\odot)$	$\alpha_{\rm sat}$	$\Delta_{\rm vir}$
1	0.10	0.95	3.81×10^{11}	1.22×10^{12}	1.04	240
2	0.16	0.90	6.27×10^{11}	1.73×10^{13}	1.03	210
3	0.30	0.80	1.17×10^{12}	2.65×10^{13}	1.04	190
4	0.47	0.69	1.87×10^{12}	3.49×10^{13}	1.05	165
5	0.63	0.60	2.41×10^{12}	3.85×10^{13}	1.09	155

NOTE. — The HOD parameters of the fiducial model (*Model 3*) are chosen to reproduce the same clustering of the SDSS galaxy sample of $M_r \leq -20$ and to match the number density of galaxies $\bar{n}_g = 5.74 \times 10^{-3}$ $(h^{-1}\mathrm{Mpc})^{-3}$. HOD parameters of the other models are scaled with Ω_m from the HOD parameters of the fiducial model and adjusted to match ξ_{gg} and $\bar{n}_g$.

contents of all halos with $M < 4.6 \times 10^{13}$ $h^{-1}M_\odot$.

Figure 3 plots the fractional difference in $\xi_{gg}(r)$, $\xi_{gm}(r)$, and $\Delta\Sigma(r)$ between the shuffled halo realizations and the original populated halos. We use the populated halos as the comparison standard rather than the SPH galaxies so that we can isolate the impact of environmental dependence of $P(N|M)$. Error bars show the error on the mean from the four shufflings, but recall that we have only one realization of the original populated halos. For $N_{\rm fix} = 5$, there is a 5% increase on $\xi_{gg}(r)$ at $r \lesssim 0.5$ $h^{-1}\mathrm{Mpc}$. However, these scales lie in the 1-halo regime where environmental variation of $P(N|M)$ should have no impact at all, so the increase is probably a statistical fluctuation that reflects the particular sizes and concentrations of the halos present in the simulation. It is only slightly larger than the 1σ error bars, and the errors from point to point are highly correlated. For $N_{\rm fix} = 20$, the changes in $\xi_{gg}(r)$ are less than 3% over the range 0.08 $h^{-1}\mathrm{Mpc} \lesssim r \lesssim 3$ $h^{-1}\mathrm{Mpc}$. The three points at $r \gtrsim 5$ $h^{-1}\mathrm{Mpc}$ are depressed by $\sim 5\%$ on average, which suggests that shuffling may slightly lower the large scale galaxy bias factor, but the statistical significance of this depression is difficult to assess with a single 50 $h^{-1}\mathrm{Mpc}$ simulation.

Shuffling changes $\xi_{gm}(r)$ by less than 5%, usually much less, except for the largest scale point with $N_{\rm fix} = 5$. Most significantly for our present purposes, the changes in $\Delta\Sigma(r)$ are at most $\sim 2\%$ for $N_{\rm fix} = 20$ at all scales, and only slightly larger for $N_{\rm fix} = 5$. We conclude that ignoring any possible environmental dependence of $P(N|M)$ has minimal impact on the calculation of galaxy-galaxy lensing observables for a given cosmology and HOD, for a galaxy sample defined by a threshold in baryonic mass. There could be a few percent effect on the large scale bias of the galaxy-galaxy correlation function, which might lead to small errors in inferring the HOD from observations of $\xi_{gg}(r)$. Assessing the importance of this effect will require larger simulations. Croton, Gao & White (2006) have carried out a similar shuffling experiment for semi-analytic galaxy populations in the 500 $h^{-1}\mathrm{Mpc}$ Millennium Run simulation (Croton et al. 2006), and they find few percent changes in large scale bias for galaxy samples defined by thresholds in mass or absolute magnitude (it was the hearing about their shuffling experiment that inspired us to carry out our own).

3. *N*-BODY SIMULATIONS

To help us develop and test our analytic model, we have carried out five *N*-body simulations of a ΛCDM universe us-

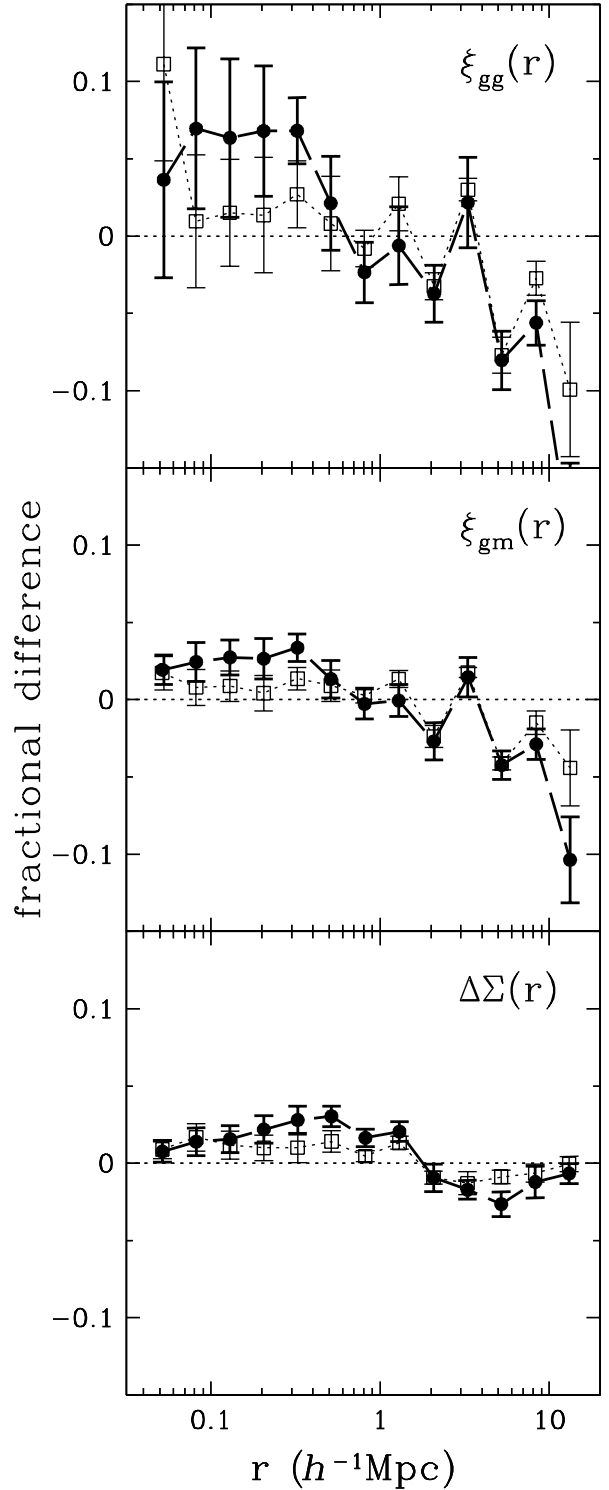FIG. 3.— Possible impact of environmental variation of the HOD on $\xi_{gg}(r)$, $\xi_{gm}(r)$, and $\Delta\Sigma(r)$. We shuffle the occupation numbers of halos of similar mass, leaving the populations of the five (*filled circles*) or 20 (*open squares*) most massive halos unchanged. Plots show the fractional difference between the shuffled halo results and the original results. Error bars in the points show the uncertainty in the mean calculated from four different shufflings (see text).
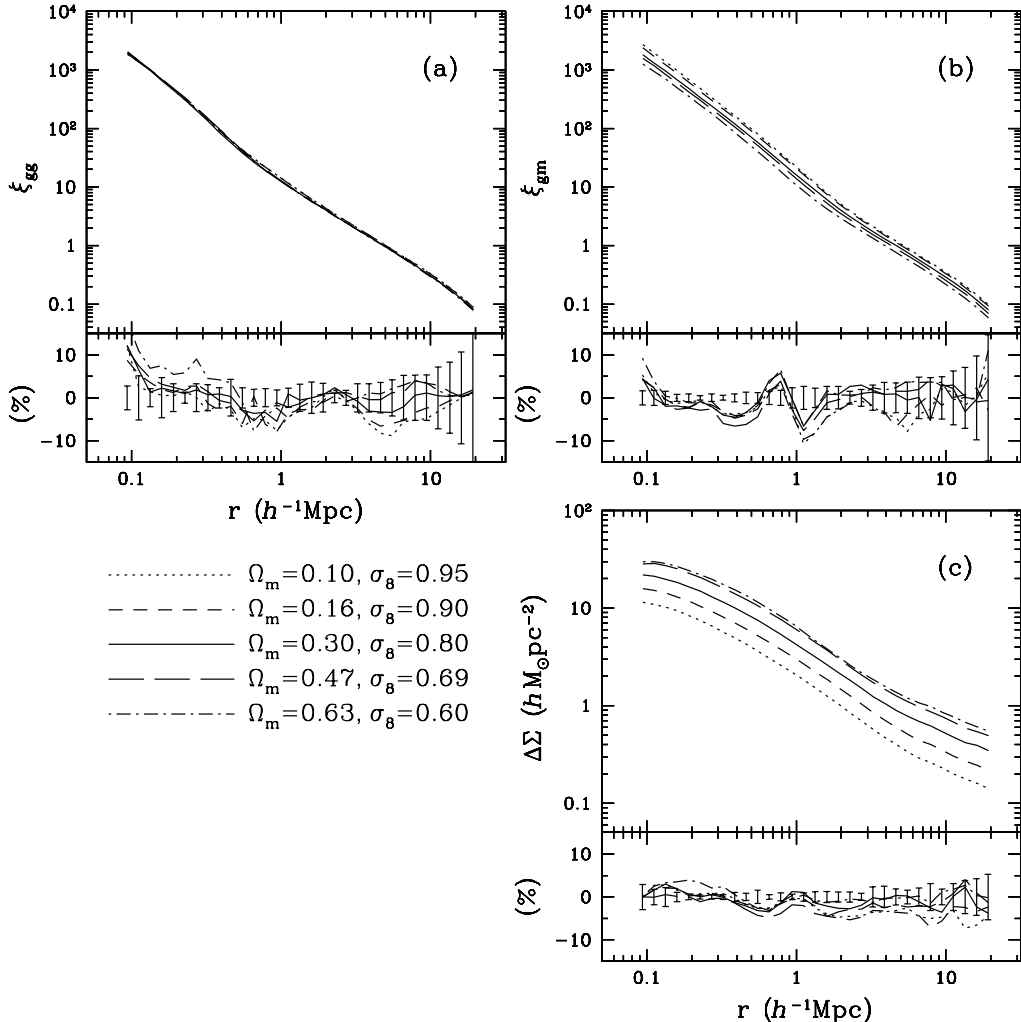
FIG. 4.— Large panels show N-body results for $\xi_{gg}(r)$, $\xi_{gm}(r)$, and $\Delta\Sigma(r)$ for the five cosmological parameter combinations indicated in the legend and detailed in Table 1. Attached bottom panels show the fractional difference between the analytic model calculations and the simulation results. Error bars represent fractional statistical uncertainty on the N-body results for the central model ($\Omega_m = 0.3$ and $\sigma_8 = 0.8$, *solid lines*), computed from the error on the mean of the five simulations.

ing GADGET (Springel et al. 2001). Each simulation begins at expansion factor $a = 0.01$ with a scale-invariant ($n = 1$) fluctuation spectrum modulated by the transfer function of Efstathiou et al. (1992) with shape parameter $\Gamma = 0.2$. Our analytic model calculations in § 5 use the CMBFAST transfer function (Seljak & Zaldarriaga 1996), which represents cosmological predictions more accurately, but the Efstathiou et al. (1992) representation should be adequate for calibrating and testing the analytic model itself. The simulations end at $a = 1.0$, when $\Omega_m = 0.1$, $\Omega_\Lambda = 0.9$, and the linear theory normalization of the power spectrum is $\sigma_8 = 0.95$. We use earlier outputs from the same simulations to represent models with the cosmological parameter combinations listed in Table 1: $(\Omega_m, \sigma_8) = (0.16, 0.90)$, $(0.30, 0.80)$, $(0.48, 0.69)$, and $(0.63, 0.60)$. Since we are adopting a fixed, observationally motivated form of the power spectrum instead of changing its shape with Ω_m, this procedure is exact. We would obtain the same results if we ran a separate simulation for each model but started it at expansion factor $a = 0.01/a_{out}$, where $a_{out} = 0.84$, 0.64, 0.49, 0.40 for the four (Ω_m, σ_8) combinations. We refer the reader to Tinker et al. (2005, 2006) for the simulation

details.

Our simulations use 360^3 particles to model a volume 253 h^{-1}Mpc (comoving) on a side. The dark matter particle mass is $9.6 \times 10^{10}\Omega_m h^{-1}M_\odot$. We choose the mass resolution so that the lowest mass halos that host galaxies with $M_r \leq -20$, according to our HOD fits (see below), contain at least 32 particles. The gravitational force resolution is $\epsilon = 70~h^{-1}$kpc (this is the approximate Plummer-equivalent value). The five simulations are identical except for the random number seed used to generate the initial conditions. We identify dark matter halos using FOF with a linking length equal to 0.2 times the mean interparticle separation, or 140 h^{-1}kpc, and set the halo mass equal to the total mass of the linked particles.

We populate the N-body halos with galaxies using HOD parameters that are designed to reproduce the mean space density and projected correlation function of SDSS galaxies with $M_r \leq -20$, as measured by Zehavi et al. (2005b). The adopted form of the HOD is motivated by the results of Kravtsov et al. (2004) and Zheng et al. (2005). Halos below some minimum mass M_{min} are devoid of galaxies. All halos above M_{min} have a central galaxy, which is placed at the position of the dark mat-

ter particle with the lowest potential energy in each halo. The number of satellite galaxies is drawn from a Poisson distribution with mean $(M/M_1)^{\alpha_{\text{sat}}}$. Each satellite galaxy is placed on a randomly selected dark matter particle from the halo. Table 1 lists the values of M_{min}, M_1, and α_{sat} for our five (Ω_m, σ_8) combinations. Further details of the fitting procedure are given by Tinker et al. (2006). The specifics of the parametrization and details of the fitting method are not important to our purposes here, since we will test the analytic model predictions using the same HOD parameters applied to the simulations. However, these parameter choices ensure a galaxy population with realistic clustering properties.

Figure 4 shows $\xi_{\text{gg}}(r)$, $\xi_{\text{gm}}(r)$, and $\Delta\Sigma(r)$ for the five N-body models. The five galaxy-galaxy correlation functions are nearly identical by construction, though with the HOD parameters at our disposal it is not possible to exactly match the observed correlation function over our full range of σ_8. The galaxy-matter correlation function is higher for the more strongly clustered, high σ_8 models, as expected. However, since $\Delta\Sigma(r)$ scales (approximately) with $\Omega_m\sigma_8$, and Ω_m falls faster than σ_8 grows in our simulation outputs, the order of models is reversed on the $\Delta\Sigma(r)$ panel. We discuss the comparison between the N-body and analytic model results in the following section.

4. ANALYTIC MODELING OF GALAXY-MATTER CLUSTERING

4.1. *Formulation and Tests*

Our analytic method of calculating $\xi_{\text{gm}}(r)$ for a given cosmology and HOD is based on the methods that Zheng (2004) and Tinker et al. (2005a, see Appendix B) used to calculate the galaxy-galaxy correlation function. These methods are based, in turn, on ideas introduced by Scherrer & Bertschinger (1991), Ma & Fry (2000), Seljak (2000), Peacock & Smith (2000) and Scoccimarro et al. (2001). We present a full technical description of our ξ_{gm} calculation here but refer the reader to these earlier works for more general discussion. Our galaxy-galaxy correlation calculations follow Tinker et al. (2005), with ellipsoidal halo exclusion.

Contributions to ξ_{gm} can come from galaxy-matter pairs[12] residing in a single halo or in two distinct halos. We separate these two contributions as

$$1 + \xi_{\text{gm}}(r) = \left[1 + \xi_{\text{gm}}^{1h}(r)\right] + \left[1 + \xi_{\text{gm}}^{2h}(r)\right], \quad (5)$$

noting that it is pair counts (proportional to $1+\xi_{\text{gm}}$) that add rather than the correlations ξ_{gm} themselves. The one-halo contribution is

$$1 + \xi_{\text{gm}}^{1h}(r) = \frac{1}{4\pi r^2 \bar{n}_g} \int_{M_{\text{min}}}^{\infty} dM \frac{dn}{dM} \langle N \rangle_M \frac{M}{\bar{\rho}_m} \frac{1}{2R_{\text{vir}}} \text{F}'\left(\frac{r}{2R_{\text{vir}}}\right), \quad (6)$$

where dn/dM is the halo mass function (Press & Schechter 1974; Sheth & Tormen 1999; Jenkins et al. 2001), $\langle N \rangle_M$ is the mean number of galaxies in halos of mass M, $\bar{\rho}_m$ is the mean mass density, and $F(r/2R_{\text{vir}})$ is the average fraction of galaxy-matter pairs in halos of mass M and virial radius R_{vir} that have separation less than r (Berlind & Weinberg 2002; $F'(x)$ is simply the derivative of $F(x)$ with respect to its argument). We define R_{vir} such that the mean density within R_{vir} is $\Delta_{\text{vir}}\bar{\rho}_m$, and unless otherwise stated we assume $\Delta_{\text{vir}} = 200$. We further split the one-halo term by discriminating central

---

[12] By which we mean pairs of galaxies and dark matter particles.

and satellite galaxies (see, e.g., Berlind & Weinberg 2002; Yang et al. 2003; Zheng 2004),

$$\langle N \rangle_M \text{F}'(x) = \langle N_{\text{cen}} \rangle_M \text{F}'_{\text{cen}}(x) + \langle N_{\text{sat}} \rangle_M \text{F}'_{\text{sat}}(x). \quad (7)$$

Pairs involving a central galaxy simply follow the radial mass profile $\rho(r)$, so $\text{F}'_{\text{cen}}(x) \propto \rho(r)r^2$. The distribution $\text{F}'_{\text{sat}}(x)$ of satellite galaxy-matter pairs is the convolution of the galaxy and matter profiles. We assume a spherical NFW profile (Navarro, Frenk & White 1997), truncated at R_{vir}, for both dark matter and satellite galaxies. We compute the dark matter concentration parameter c_{dm} using the relation of Bullock et al. (2001). We allow the galaxy concentration to be different, $c_{\text{gal}} = \alpha_c c_{\text{dm}}$, but adopt $\alpha_c = 1$ as our standard assumption.

On scales much larger than the virial diameter of the largest halo, the galaxy-matter correlation function is equal to $\xi_{\text{mm}}(r)$ multiplied by a galaxy bias factor

$$b_{\text{gal}} = \frac{1}{\bar{n}_g} \int_0^{\infty} dM \frac{dn}{dM} \langle N \rangle_M b_{\text{h}}(M), \quad (8)$$

where $b_{\text{h}}(M)$ is the bias factor of halos of mass M. However, an accurate calculation on intermediate scales must account for the finite extent of halos, for the scale dependence of $b_{\text{h}}(M)$, and for halo exclusion — two spherical halos cannot be separated by less than the sum of their virial radii. It is convenient to do the calculation in Fourier space, where the convolutions of halo profiles become multiplications of their Fourier transforms. Our complete series of expressions for the two-halo contribution to $\xi_{\text{gm}}(r)$ is

$$1 + \xi_{\text{gm}}^{2h}(r) = \left(\frac{\bar{n}'_g}{\bar{n}_g}\right) \left[1 + \xi_{\text{gm}}^{2h'}(r)\right], \quad (9)$$

where

$$\xi_{\text{gm}}^{2h'}(r) = \frac{1}{2\pi^2} \int_0^{\infty} dk k^2 P_{\text{gm}}^{2h'}(k|r) \frac{\sin(kr)}{kr}, \quad (10)$$

is the Fourier transform of

$$P_{\text{gm}}^{2h'}(k|r) = P_m(k)\frac{1}{\bar{n}'_g} \int_0^{\infty} dM_1 \frac{dn}{dM_1} \langle N \rangle_{M_1} b_{\text{h}}(M_1|r)\, y_g(k, M_1)$$

$$\times \int_0^{\infty} dM_2 \frac{dn}{dM_2} \frac{M_2}{\bar{\rho}_m} b_{\text{h}}(M_2|r)\, y_m(k, M_2)\, p_{\text{no}}(x|M_1, M_2), \quad (11)$$

where $y_g(k, M)$ and $y_m(k, M)$ are the normalized Fourier counterparts of the galaxy and the matter profiles, and

$$\bar{n}_g'^2 = \int_0^{\infty} dM_1 \frac{dn}{dM_1} \langle N \rangle_{M_1} \int_0^{\infty} dM_2 \frac{dn}{dM_2} \langle N \rangle_{M_2} p_{\text{no}}(x|M_1, M_2). \quad (12)$$

In these expressions, $p_{\text{no}}(x|M_1, M_2)$ represents the probability that two halos of mass M_1 and M_2 with scaled separation $x \equiv r/(R_{\text{vir},1} + R_{\text{vir},2})$ do not overlap. For spherical halos, $p_{\text{no}}(x)$ would be a step function at $x = 1$, but Tinker et al. (2005) found that an accurate separation of the 1-halo and 2-halo contributions to $\xi_{\text{gg}}(r)$ requires accounting for the non-spherical shapes of halos identified by the FOF algorithm. We adopt their expression, based on a fit to Monte Carlo realizations of ellipsoidal halo pairs with a reasonable distribution of axis ratios: $p_{\text{no}}(x) = 0$ for $x < 0.8$, $p_{\text{no}}(x) = 1$ for $x > 1.09$, and $p_{\text{no}}(x) = (3y^2 - 2y^3)$ with $y = (x - 0.8)/0.29$ for $0.8 \leq x \leq 1.09$. The restricted number density n'_g is the mean space density of galaxies residing in allowed (i.e., non-overlapping) halo pairs at separation r. Since $p_{\text{no}}(x|M_1, M_2)$ and the halo bias factors $b_{\text{h}}(M|r)$ depend on r, one must evaluate equations (9)–(12)

separately for each value of r where one wants to know $\xi_{gm}(r)$. The double integrals in equations (11) and (12) are non-separable because of the M_1-dependence of $p_{no}(x)$. In principle, one should separately compute equation (11) for central and satellite galaxies and sum the results, since $y_g(k, M)$ is different in the two cases, but we have tested and found that ignoring this subtlety has negligible effect.

For scale-dependent halo bias factors, we adopt the expression

$$b_h^2(M|r) = b_{asym}^2(M) \times \frac{[1 + 1.17\xi_{mm}(r)]^{1.49}}{[1 + 0.69\xi_{mm}(r)]^{2.09}} , \quad (13)$$

from Tinker et al. (2005). We also use Tinker et al.'s (2005a; Appendix A) expressions for the asymptotic bias factors $b_{asym}(M)$. These follow the formulation of Sheth et al. (2001b), but with different parameter values that yield a substantially better fit to the simulations. For "concordance" cosmological parameters, these bias factors are similar to those of Seljak & Warren (2004), but they are more accurate for models with different matter power spectra. We use Smith et al.'s (2003) approximation for the non-linear power spectrum $P_{mm}(k)$ and correlation function $\xi_{mm}(r)$ in equations (11) and (13). One could in principle use $P_{lin}(k)$ instead of $P_{mm}(k)$; this would require a different (though still scale-dependent) expression for $b_h(M|r)$ with a separate N-body calibration.

The calculation as we have described it is a straightforward generalization of the $\xi_{gg}(r)$ calculation presented by Tinker et al. (2005), who tested its accuracy over the range $\sigma_8 = 0.6 - 0.95$ for both the $\Gamma = 0.2$ simulations used here and for a similar set with $\Gamma = 0.12$. However, a significant technical, and to some degree conceptual issue arises with the evaluation of the second integral in equation (11). Since we assign all galaxy-matter pairs to either the 1-halo or 2-halo terms, we implicitly assume that all dark matter is in halos of some mass, and thus

$$\int_0^\infty dM \frac{dn}{dM} M = \bar{\rho}_m. \quad (14)$$

More importantly for present purposes, the distribution of matter is by definition unbiased with respect to itself, and therefore

$$\int_0^\infty dM \frac{dn}{dM} \frac{M}{\bar{\rho}_m} b_h(M|r) = 1. \quad (15)$$

The Jenkins et al. (2001) mass function and Tinker et al. (2005) halo bias factors used here are fits to simulations over a finite range of halo masses, and they do not satisfy either of these constraints. To impose the constraint (15) explicitly, we break the second integral of equation (11) at a halo mass $M_{brk} = 10^8 \ h^{-1}M_\odot$ and evaluate it as

$$\int_0^\infty dM_2 \frac{dn}{dM_2} \frac{M_2}{\bar{\rho}_m} b_h(M_2|r) \, y_m(k, M_2) p_{no}(x|M_1, M_2)$$

$$\approx \int_{M_{brk}}^\infty dM_2 \frac{dn}{dM_2} \frac{M_2}{\bar{\rho}_m} b_h(M_2|r) \, y_m(k, M_2) p_{no}(x|M_1, M_2)$$

$$+ \left[1 - \int_{M_{brk}}^\infty dM' \frac{dn}{dM'} \frac{M'}{\bar{\rho}_m} b_h(M'|r) \right]. \quad (16)$$

For the term in brackets on the right hand side, we make the (good) approximation that $p_{no}(x) = y(k, M) = 1$ for halos with $M < M_{brk}$ at all radii of interest for our calculation, then apply equation (15). We find that this procedure is necessary to

obtain accurate results. The same problem does not arise for integrals involving $\langle N \rangle_M$ because the mean occupation itself goes to zero at low halo masses.

We must make one further adjustment to the analytic model before testing it against the populated N-body halos described in § 3. These halos are identified by the FOF algorithm, which, roughly speaking, selects particles within an isodensity surface. The *mean* overdensity Δ_{vir} within this surface depends on the halo profiles. To compute the effective value of Δ_{vir} for our simulations, we calculate the mean density within spheres centered on the most-bound particles of the FOF halos that enclose the halo's FOF mass. The canonical value of $\Delta_{vir} = 200$ is accurate for our central model with $\Omega_m = 0.3$ and $\sigma_8 = 0.8$. However, the Δ_{vir} values for other models, listed in Table 1, deviate by up to 20%. The trend is as expected: halos in low Ω_m models are more concentrated because they form earlier, and they have higher values of Δ_{vir}. However, the Ω_m-dependence of FOF halos selected with constant linking parameter is much weaker than the variation of virial densities predicted by the spherical collapse model (e.g., Bryan & Norman 1998). When calculating virial radii as a function of halo mass, we use the Δ_{vir} values in Table 1.

The attached bottom frame in Figure 4a shows the fractional difference between the analytic model and N-body results for the galaxy-galaxy correlation function, $(\xi_{analytic} - \xi_{N-body})/\xi_{N-body}$, for the five cosmological/HOD models listed in Table 1. Error bars represent the statistical uncertainty in the mean value of ξ_{N-body}, computed from the dispersion among the five independent simulations; for clarity, we show these only for the central model with $\Omega_m = 0.3$. The differences between the analytic and numerical results are usually less than 5% at all $r > 0.1 \ h^{-1}$Mpc. The one deviation that is clearly statistically significant is the rapid turn-up of the residuals at $r \simeq 0.1 \ h^{-1}$Mpc, which reflects the smoothing effect of the simulation's gravitational force softening. The marginally significant, $\sim 5\%$ discrepancy at $r \simeq 0.8 \ h^{-1}$Mpc suggests that our ellipsoidal exclusion correction still underestimates the number of close halo pairs, even though it allows halos to be separated by less than the sum of their virial radii. Without this correction, the deviation would fall off the bottom of the plot (see Fig. 10 in Tinker et al. 2005). The $\sim 8\%$ divergence of the models at $r \simeq 8 \ h^{-1}$Mpc results from the deviations of the Smith et al. (2003) non-linear matter power spectrum from our simulation results. This difference could be partly an artifact of our finite box size, but the systematic dependence on cosmological parameters and reconvergence of results at $r = 20 \ h^{-1}$Mpc suggest that it is mostly a result of slight non-universality of the Smith et al. (2003) formula, though it is hard to reach a definitive conclusion because of the substantial statistical uncertainties at these scales.

The bottom frames in Figure 4b and 4c show equivalent fractional differences for $\xi_{gm}(r)$ and $\Delta\Sigma(r)$. The residuals for $\xi_{gm}(r)$ are similar to those for $\xi_{gg}(r)$, with the rise at $r \simeq 0.1 \ h^{-1}$Mpc, again reflecting the force softening in the numerical simulation. Since $\Delta\Sigma(r)$ depends on ξ_{gm} at all separations less than r (see eq.[3]), and the deviation between analytic and N-body ξ_{gm} grows at smaller separations, a comparison between the pure analytic calculation and the measurement of $\Delta\Sigma(r)$ from the simulation shows a substantial offset at $r \lesssim 1 \ h^{-1}$Mpc. However, this offset reflects the limited resolution of the N-body simulation, not the failure of the analytic model. (Similar deviations at small scale were found by Mandelbaum et al. 2005.) To remove this numerical arti-

fact from the comparison, we set $\Delta\Sigma$ for the analytic model equal to the N-body value at $r = 0.1\ h^{-1}$Mpc, then use the analytic calculation of $\xi_{gm}(r)$ to obtain the surface density for $r > 0.1\ h^{-1}$Mpc. With this correction, the analytic model for $\Delta\Sigma(r)$ is accurate to 5% or better for all five cosmological models at all radii $0.1\ h^{-1}$Mpc $\leq r \leq 20\ h^{-1}$Mpc.

4.2. *Dissection of Correlation Functions*

It is interesting to examine the separate contributions of central and satellite galaxies to the galaxy-galaxy and galaxy-matter correlation functions. Figure 5a shows the familiar decomposition of $\xi_{gg}(r)$ into 1-halo and 2-halo contributions (see Berlind & Weinberg 2002 for extensive discussion). We adopt the fiducial model with $\Omega_m = 0.3$, $\sigma_8 = 0.8$, and the corresponding HOD parameters listed in Table 1, and we use the N-body simulation measurements. The 1-halo term dominates at small scales, but it drops rapidly towards larger r as halos with large virial diameters become increasingly rare. At large scales, the 2-halo term is a linearly biased version of the matter correlation function, but at small scales it turns over and drops because of halo exclusion. We plot $1 + \xi(r)$ rather than $\xi(r)$ itself because pair counts are additive, so individual contributions sum to give the total $1 + \xi(r)$; this consideration becomes especially important for the central-satellite decompositions shown in subsequent panels. The transition between 1-halo and 2-halo dominance occurs at roughly the virial diameter of $M_\star$ halos, where $M_\star$ is the characteristic scale of the halo mass function.

Figure 5b separates $1 + \xi_{gg}(r)$ into central and satellite galaxy contributions. Central-satellite pairs dominate $\xi_{gg}(r)$ at $r \lesssim 0.4\ h^{-1}$Mpc, and central-central pairs at $r \gtrsim 1\ h^{-1}$Mpc, while satellite-satellite pairs dominate by a small factor in the intermediate regime. Figure 5c and 5d show the separate central and satellite contributions to the 1-halo and 2-halo terms, revealing the origin of the behavior in Figure 5b. Central-satellite pairs dominate $\xi^{1h}(r)$ at small scales because in this regime most pairs come from the most common halos that are large enough to host a galaxy pair. These halos have $\langle N \rangle_M < 3$, and they therefore have more central-satellite galaxy pairs than pairs that involve only satellites. Conversely, satellite-satellite pairs dominate $\xi^{1h}(r)$ at large scales because the halos with virial diameters large enough to host pairs at these separations have $\langle N \rangle_M > 3$. Finally, pairs involving at least one central galaxy dominate the 2-halo term by a large factor at all separations, because only halo pairs in which *both* halos have $\langle N \rangle_M > 2$ contribute, on average, more satellite-satellite pairs than central-central or central-satellite pairs. Such halos are much less common than those with $1 \leq \langle N \rangle_M \leq 2$. Thus, satellite-satellite pairs make a major contribution to the total $\xi_{gg}(r)$ only over the radial range in which 1-halo contributions from high mass halos are dominant.

Figure 6 shows the equivalent dissection of $\xi_{gm}(r)$. The overall behavior is very similar to that seen in Figure 5. The 2-halo term extends to somewhat smaller scales because halos with mass near M_{min} can still form galaxy-matter pairs with lower mass halos that have smaller virial radii. The satellite contribution to the 2-halo term is analogous to the sum of central-satellite and satellite-satellite pairs for $\xi_{gg}(r)$ because there are no "central" dark matter particles. (The normalization is lower than in Figure 2 because we now calculate the expected number of galaxy-matter pairs using all galaxies instead of satellites alone.) However, it is still a factor of 3−5

below the central 2-halo term at nearly all separations. From Figure 6, we can understand why the individual halos of satellite galaxies appear to have so little impact on the SPH results discussed in § 2. Satellite galaxies dominate the 1-halo term of $\xi_{gm}(r)$ only beyond $r \simeq 0.25\ h^{-1}$Mpc. However, the individual halos of satellites orbiting in larger groups are usually tidally truncated well inside this radius, on scales where the signal is swamped by the contribution from central galaxies. Note that the satellite fraction of galaxy samples is typically less than 30%, and hence the lensing signal of satellite galaxies is smaller by an order of magnitude than that of central galaxies. The dark halos of satellites in groups and clusters can be measured by galaxy-galaxy lensing (Natarajan et al. 2002), but only by first identifying satellites and measuring $\Delta\Sigma(r)$ for them specifically.

5. FROM GALAXY-GALAXY LENSING TO COSMOLOGICAL PARAMETERS

Having established the accuracy of the analytic model, we can now use it to investigate the dependence of $\Delta\Sigma(r)$ on Ω_m and σ_8. We consider a well-defined sample of galaxies, choose HOD parameters for each (Ω_m, σ_8) combination by fitting the mean space density and projected correlation function of this sample, then predict $\Delta\Sigma(r)$. In this section, we focus on the sample of SDSS galaxies with $M_r \leq -21$, with the projected correlation function, error covariance matrix, and mean space density $\bar{n}_g = 1.17 \times 10^{-3}\ h^3 \text{Mpc}^{-3}$ taken from Zehavi et al. (2005b). We also present predictions for a fainter luminosity threshold, $M_r \leq -20$, again using Zehavi et al. (2005b)'s observational constraints.[13] At large scales, we expect to recover the linear theory, linear bias result, $\Delta\Sigma \propto \Omega_m/b \propto \sigma_8\Omega_m$, but we can extend the predictions to intermediate and small scales using the full analytic model.

We make two significant changes in our application of the analytic model. First, we use a CMBFAST transfer function (Seljak & Zaldarriaga 1996), computed for $\Omega_m = 0.3$, $h = 0.7$, $\Omega_b = 0.04$, in place of the Efstathiou et al. (1992) parametrization adopted in our N-body simulations. This change to the transfer function has little effect on the HOD parameters inferred by fitting $w_p(r_p)$, but it has a noticeable effect on the χ^2 values of these fits, and it affects the $\Delta\Sigma(r)$ predictions themselves. Note that we do *not* change the transfer function when changing Ω_m from our fiducial value of 0.3; because the power spectrum shape is empirically well constrained, we assume that any effect of changing Ω_m will be compensated by adjusting h, Ω_b, or the inflationary index n (which we set to one). Second, we define halo virial radii assuming $\Delta_{vir} = 200$ for all Ω_m, instead of the varying Δ_{vir} values listed in Table 1 and used in § 4. This change simply amounts to a slight change in the halo definition; to identify these halos in N-body simulations, one would need to adjust the FOF linking length slightly with Ω_m. The Bullock et al. (2001) concentration parameters are defined for different (Ω_m-dependent) Δ_{vir} values, but we rescale them to our Δ_{vir} definition. We still adopt the Jenkins et al. (2001) halo mass function for all cosmological models, with no rescaling.

Figure 7 illustrates the results for a sequence of models with σ_8 ranging from 0.6 to 1.0, all for $\Omega_m = 0.3$. The HOD parameter values required to match the Zehavi et al. (2005b) $w_p(r_p)$ measurements are listed in Table 2, and the mean occupation functions $\langle N \rangle_M$ are shown in panel 7a. For lower σ_8, matching

---

[13] Specifically, we use the Zehavi et al. (2005b) measurements for the $M_r \leq -20$ sample with limiting redshift $z = 0.06$.
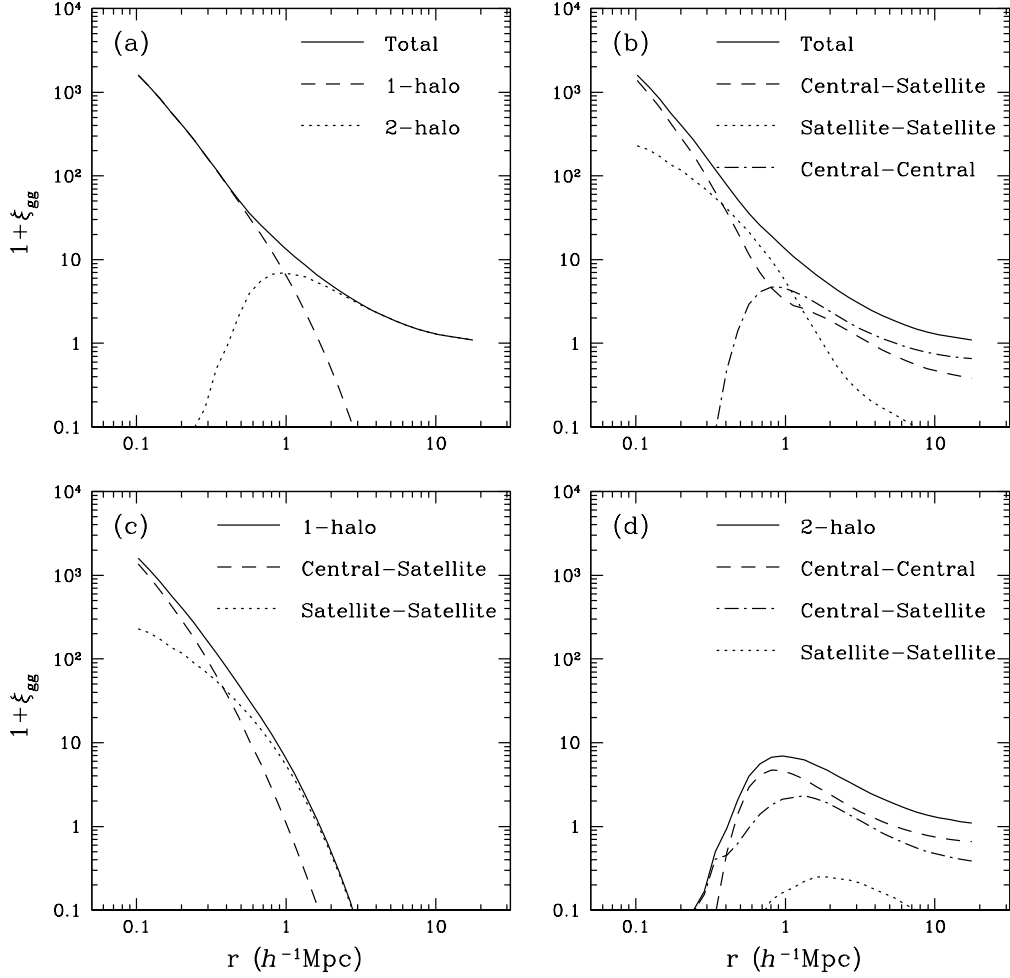
FIG. 5.— Dissection of the galaxy-galaxy correlations for the fiducial model. (a) Contributions of one-halo (*dashed*) and two-halo (*dotted*) galaxy pairs to the full correlation function (*solid*). (b) Contributions of central-satellite (*dashed*), satellite-satellite (*dotted*), and central-central (*dot-dashed*) galaxy pairs. Panels (c) and (d) show the central/satellite decompositions of the one- and two-halo terms individually.

the observed clustering requires a larger fraction of galaxies in more massive, more biased halos, hence higher values of the $\langle N_{\mathrm{sat}}\rangle_M$ slope α_{sat}. The resulting galaxy correlation functions are very similar for all five values of σ_8, as shown in Figure 7d. Figure 7b plots $(M/\bar{\rho}_m)\, dn/d\ln M$, the fraction of mass contained in a (natural) logarithmic bin centered at mass M. For $\sigma_8 = 0.6$, this function peaks near $M \sim 10^{13}\, h^{-1} M_\odot$, while for $\sigma_8 = 1.0$ it peaks near $M \sim 10^{14}\, h^{-1} M_\odot$. Figure 7c plots the same function multiplied by $\langle N\rangle_M$, a product that is proportional to the number of 1-halo galaxy-matter *pairs* that arise in halos of mass M. This function peaks at $M \sim 3 \times 10^{14}\, h^{-1} M_\odot$ for $\sigma_8 = 0.6$ and $M \sim 10^{15}\, h^{-1} M_\odot$ for $\sigma_8 = 1.0$. The trend of α_{sat} with σ_8 partly compensates the trend of the mass distribution in Figure 7b, reducing the order-of-magnitude shift in the peak location to a factor of three. While high mass halos near the peak contribute a substantial fraction of all galaxy-matter pairs, these pairs are spread over a larger projected area, so the contribution in a given $r \sim r + dr$ bin is multiplied by an additional factor that scales roughly as $R_{\mathrm{vir}}^{-2} \sim M^{-2/3}$. For all values of σ_8, the fraction of 1-halo galaxy-matter pairs is tiny for $M \geq 5 \times 10^{15}\, h^{-1} M_\odot$.

TABLE 2
HOD PARAMETERS FOR DIFFERENT σ_8 MODELS

Model	Ω_m	σ_8	$M_{\min}(h^{-1}M_\odot)$	$M_1(h^{-1}M_\odot)$	α_{sat}
1	0.3	0.6	4.04×10^{12}	6.28×10^{13}	1.52
2	0.3	0.7	4.46×10^{12}	7.98×10^{13}	1.40
3	0.3	0.8	4.71×10^{12}	9.58×10^{13}	1.31
4	0.3	0.9	4.85×10^{12}	1.11×10^{14}	1.25
5	0.3	1.0	4.95×10^{12}	1.23×10^{14}	1.19

NOTE. — The HOD parameters are chosen to reproduce the same clustering of the SDSS galaxy sample of $M_r \leq -21$ and to match the number density of galaxies $\bar{n}_g = 1.17 \times 10^{-3}\, (h^{-1}\mathrm{Mpc})^{-3}$.

Figures 7e and 7f show the galaxy-matter correlation functions and excess surface density profiles, respectively, for this model sequence. At large scales, $\xi_{\mathrm{gm}}(r)$ and $\Delta\Sigma(r)$ increase with $\sigma_8 \propto 1/b$ as expected from linear theory. A similar increase appears on small scales because of the larger fraction of
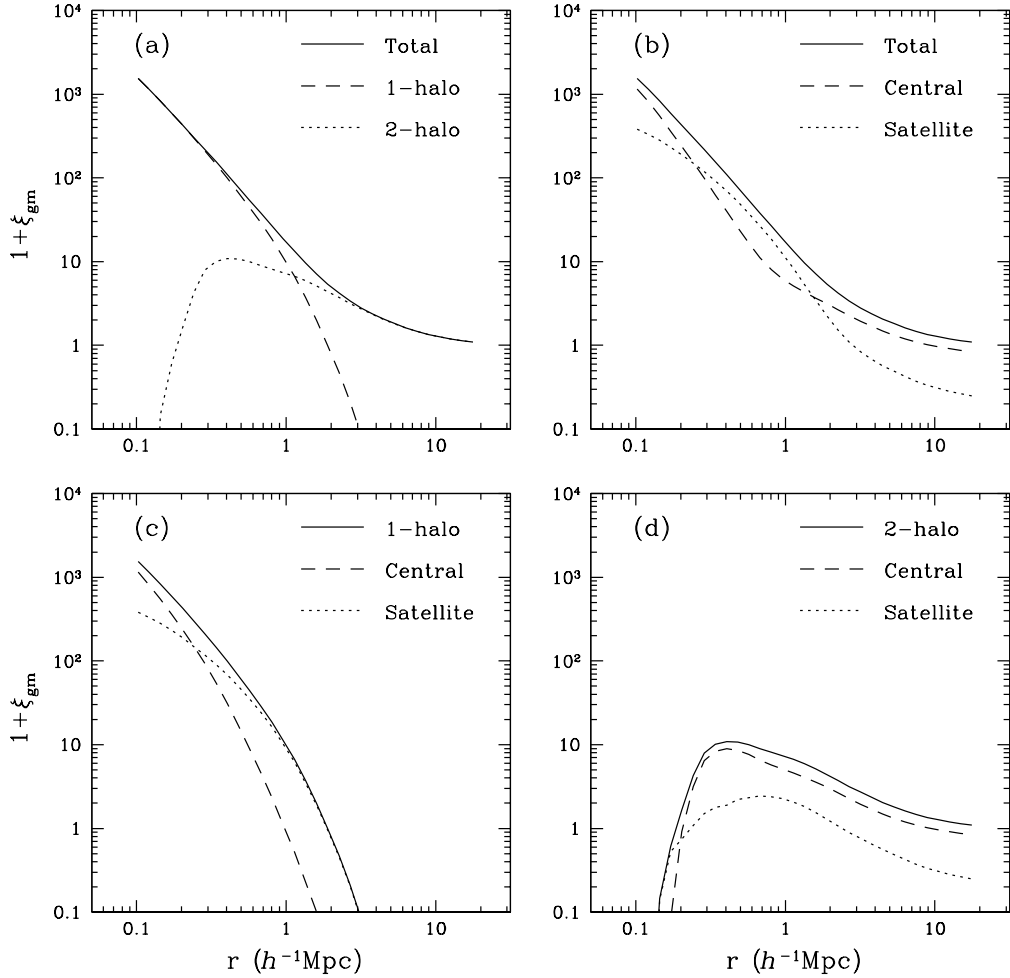
FIG. 6.— Dissection of the galaxy-matter correlations for the fiducial model, in the same format as Fig. 5. In panel (b)-(d), dashed and dotted lines show galaxy-matter pairs involving a central galaxy or a satellite galaxy, respectively.

galaxy-matter pairs in more massive halos. In fact, the shapes of $\xi_{gm}(r)$ and $\Delta\Sigma(r)$ appear remarkably constant over the full range $0.1 \ h^{-1}\mathrm{Mpc} \leq r \leq 20 \ h^{-1}\mathrm{Mpc}$, a point we quantify below.

Figure 8 shows $\Delta\Sigma(r)$ for three model sequences with different variations. In Figure 8a, we consider the same sequence of increasing σ_8, fixed Ω_m shown in Figure 7, but we always keep halo concentrations fixed at the values predicted for $\sigma_8 = 0.8$. We adjust HOD parameters slightly from the values listed in Table 2 to obtain the minimum-χ^2 fit to the projected correlation function with the new halo concentrations. In the large r, 2-halo regime, $\Delta\Sigma(r)$ is nearly identical to that shown in Figure 7f. However, fixing the concentrations to those of the central model has an important effect at small scales, causing the $\Delta\Sigma(r)$ curves to converge. The constancy of shape in Figure 7f is thus partly a consequence of the changes in halo concentrations in different σ_8 models; higher σ_8 leads to earlier halo collapse and higher concentration, boosting $\Delta\Sigma(r)$.

Figure 8b shows a sequence with fixed $\sigma_8 = 0.8$ and Ω_m varying from 0.2 to 0.4 in steps of 0.05. For this sequence, the HOD parameters $M_{\min}$ and M_1 scale in proportion to Ω_m,

though we again make slight adjustments to fit $w_p(r_p)$. If halo concentrations were independent of Ω_m, and we did not make those small adjustments, then $\xi_{gg}(r)$ and $\xi_{gm}(r)$ would be identical for all five models after this mass rescaling, since the halo mass function and halo bias factors are functions of $M/M_\star$ and $M_\star \propto \Omega_m$ (see Zheng et al. 2002 for further discussion). In this case, $\Delta\Sigma(r)$ would have a constant shape and an amplitude proportional to Ω_m. Figure 8b shows roughly this behavior, but the trend of higher concentration for lower Ω_m produces a weak convergence of models at small r.

We have so far assumed that satellite galaxies trace the dark matter in halos, with the same NFW radial profile. We now relax this assumption and allow the satellite profiles to have a lower concentration parameter, as suggested by some numerical studies (see § 2 and Nagai & Kravtsov 2005). Figure 8c compares models with $\Omega_m = 0.3$, $\sigma_8 = 0.8$, and satellite concentration parameters $c_{gal} = \alpha_c c_{dm}$ with $\alpha_c = 0.3, 0.5, 0.7$, and 1.0. We again adjust HOD parameters to fit $w_p(r_p)$ after changing galaxy concentrations. These adjustments partly compensate for the changes in galaxy concentration, so the effect of a radial profile change is somewhat smaller here than in § 2 (Fig. 1), where we kept other HOD parame-
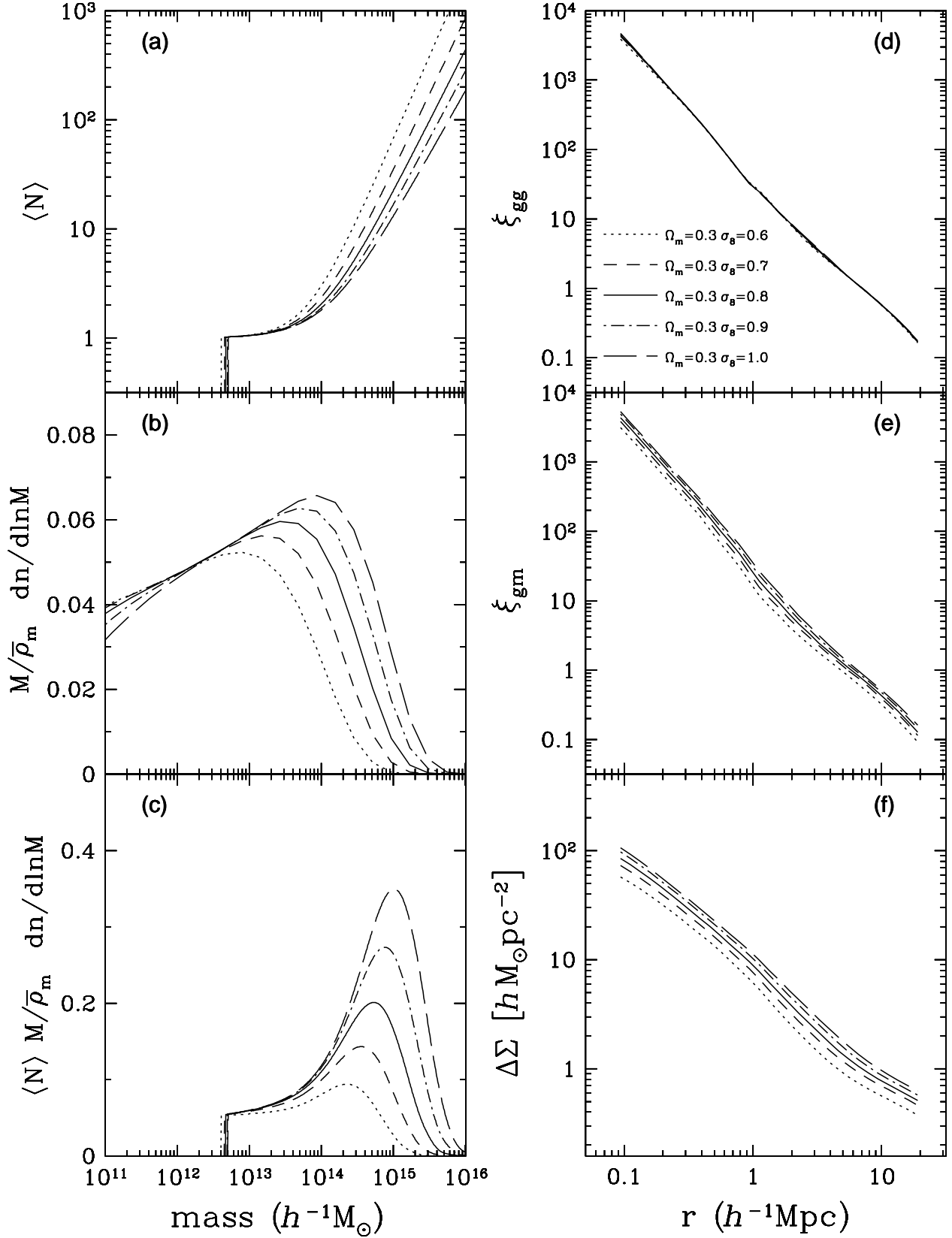
FIG. 7.— Clustering contributions and clustering signals for the model sequence with fixed Ω_m and varying σ_8. (a) Mean halo occupation functions, determined by fitting the $w_p(r_p)$ data, with σ_8 increasing from top to bottom (see panel d legend). (b) Fraction of matter per logarithmic bin of halo mass. (c) Fraction of galaxy-matter pairs per logarithmic bin of halo mass. Note that pairs in higher mass halos are spread over a wider range of separations, diluting the contribution to any given $r \rightarrow r+dr$ bin. Panel (d), (e), and (f) show the galaxy-galaxy correlation function, galaxy-matter correlation function, and excess surface density, respectively.
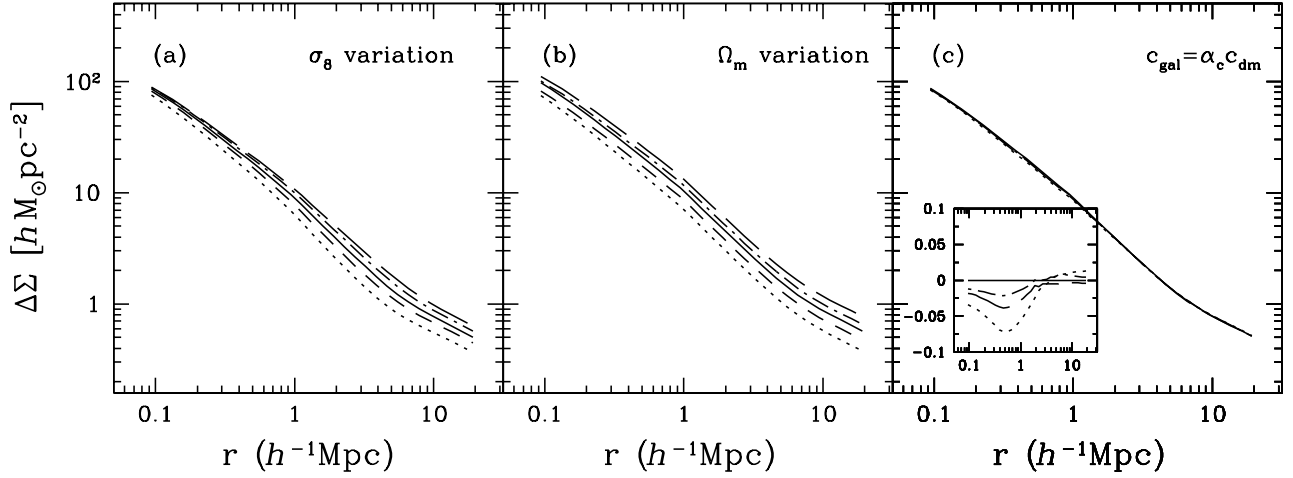
FIG. 8.— Excess surface density profiles for other model sequence. We consider (a) the same model sequence as in Fig. 7, but with halo concentrations held fixed at the values for $\Omega_m = 0.3$ and $\sigma_8 = 0.8$, (b) a sequence of models with fixed $\sigma_8 = 0.8$ and Ω_m ranging from 0.2 (*dotted*) to 0.4 (*long dashed*) in steps of 0.05, and (c) models with $\Omega_m = 0.3$ and $\sigma_8 = 0.8$ in which galaxy profile concentrations satisfy $c_{gal} = \alpha_c c_{dm}$, with $\alpha_c = 0.3$ (*dotted*), 0.5 (*long-dashed*), 0.7 (*dot-dashed*), and 1.0 (*solid*). The inset panel shows fractional deviations from the $\alpha_c = 1.0$ model.

ters fixed. For $\alpha_c \geq 0.7$, the impact on $\Delta\Sigma(r)$ is under 3% at all r. For $\alpha_c = 0.3$, the effect rises to 7% at the scale $r \sim 0.5 - 1$ h^{-1}Mpc where satellite galaxies make a dominant contribution to $\xi_{gm}(r)$ (see Fig. 6b). Small differences between galaxy and dark matter concentrations can thus be safely neglected, but large differences can have a small but measurable impact at $r < 2$ h^{-1}Mpc.

Observational studies of galaxy-galaxy lensing often examine the ratio $\xi_{gm}(r)/\xi_{gg}(r)$, which is equal to r_{gm}/b in the linear bias model (e.g., Hoekstra et al. 2001, 2002; Sheldon et al. 2004). Figure 9 plots this ratio for the four model sequences shown in Figures 7 and 8. Figure 9a shows the fixed-Ω_m, increasing σ_8 sequence of Figure 7. Since HOD parameters in each model are adjusted to match the projected correlation, model differences are driven almost entirely by changes in $\xi_{gm}(r)$. At large scales, the ratio $\xi_{gm}(r)/\xi_{gg}(r)$ is constant as predicted for linear bias, and $\xi_{gm}(r)$ increases in proportion to $\sigma_8 \propto 1/b$. Comparison to the bias factor defined by $b^2 \simeq \xi_{gg}(r)/\xi_{mm}(r)$ implies a cross-correlation coefficient $r_{gm} \simeq 0.9$ for all five models. However, in every case $\xi_{gm}(r)/\xi_{gg}(r)$ rises sharply at a scale $r \sim 1$ h^{-1}Mpc near the 1-halo to 2-halo transition. For $\xi_{gg}(r)$, this transition is fairly sharp, producing measurable deviations from a power-law (Berlind & Weinberg 2002; Zehavi et al. 2004). These deviations are smoothed out in $\xi_{gm}(r)$ because the contribution of halos below M_{min} allows the 2-halo term to overlap more with the 1-halo term (compare Figs. 5a and 6a), and the ratio $\xi_{gm}(r)/\xi_{gg}(r)$ therefore shows a sharp feature reflecting the break in $\xi_{gg}(r)$. For higher σ_8, the 1-halo term extends to larger r, and the jump in $\xi_{gm}(r)/\xi_{gg}(r)$ is larger in amplitude but spread over a larger range of r. The break in $\xi_{gg}(r)$ is generally stronger for more strongly clustered galaxy samples (Berlind & Weinberg 2002; Zehavi et al. 2005b), and we expect similar sample dependence for the $\xi_{gm}(r)/\xi_{gg}(r)$ jump.

At small scales, $\xi_{gm}(r)/\xi_{gg}(r)$ is again roughly flat, but at a level higher than the large scale ratio. As noted earlier, fixing halo concentrations causes the galaxy-matter correla-

TABLE 3
THE WEAK LENSING SIGNAL

	$M_r \leq -21$			$M_r \leq -20$		
$\log r$	$\log \Delta\Sigma(r)$	α	β	$\log \Delta\Sigma(r)$	α	β
−1.029	1.929	0.65	1.13	1.582	0.71	0.84
−0.952	1.870	0.68	1.10	1.513	0.73	0.83
−0.875	1.808	0.71	1.08	1.446	0.75	0.83
−0.798	1.743	0.73	1.06	1.378	0.77	0.83
−0.721	1.674	0.76	1.04	1.310	0.79	0.85
−0.643	1.602	0.79	1.03	1.244	0.81	0.85
−0.567	1.529	0.80	1.03	1.181	0.83	0.87
−0.489	1.453	0.83	1.03	1.116	0.84	0.91
−0.412	1.379	0.85	1.02	1.050	0.86	0.96
−0.335	1.306	0.87	1.03	0.982	0.88	1.00
−0.258	1.227	0.89	1.06	0.922	0.89	1.08
−0.181	1.145	0.91	1.10	0.860	0.91	1.13
−0.104	1.064	0.92	1.15	0.806	0.92	1.16
−0.027	0.983	0.93	1.19	0.753	0.95	1.19
0.050	0.891	0.94	1.24	0.686	0.96	1.24
0.127	0.793	0.95	1.31	0.610	0.98	1.31
0.204	0.697	0.96	1.37	0.535	0.99	1.38
0.281	0.604	0.98	1.41	0.456	1.00	1.44
0.358	0.511	0.99	1.45	0.378	1.01	1.49
0.435	0.419	1.00	1.48	0.297	1.02	1.53
0.512	0.330	1.00	1.49	0.218	1.03	1.55
0.589	0.244	1.01	1.47	0.137	1.04	1.55
0.666	0.162	1.02	1.43	0.059	1.04	1.51
0.743	0.089	1.03	1.37	−0.013	1.05	1.43
0.820	0.021	1.04	1.29	−0.076	1.05	1.35
0.897	−0.039	1.03	1.21	−0.131	1.06	1.27
0.974	−0.094	1.05	1.14	−0.196	1.05	1.20
1.051	−0.145	1.05	1.09	−0.242	1.05	1.15
1.128	−0.193	1.05	1.06	−0.288	1.05	1.12
1.205	−0.241	1.04	1.05	−0.333	1.04	1.12
1.282	−0.292	1.04	1.05	−0.382	1.04	1.12

NOTE. — The excess surface densities $\Delta\Sigma_{FID}$ of the fiducial model ($\Omega_m = 0.3$, $\sigma_8 = 0.8$) for SDSS galaxy samples of $M_r \leq -21$ and $M_r \leq -20$. The projected radius r is in h^{-1}Mpc, and $\Delta\Sigma$ is in $hM_\odot$pc^{-2}.

tion function of different σ_8 models to converge (Fig. 8a), so the $\xi_{gm}(r)/\xi_{gg}(r)$ ratios also converge in this case (Fig. 9b).
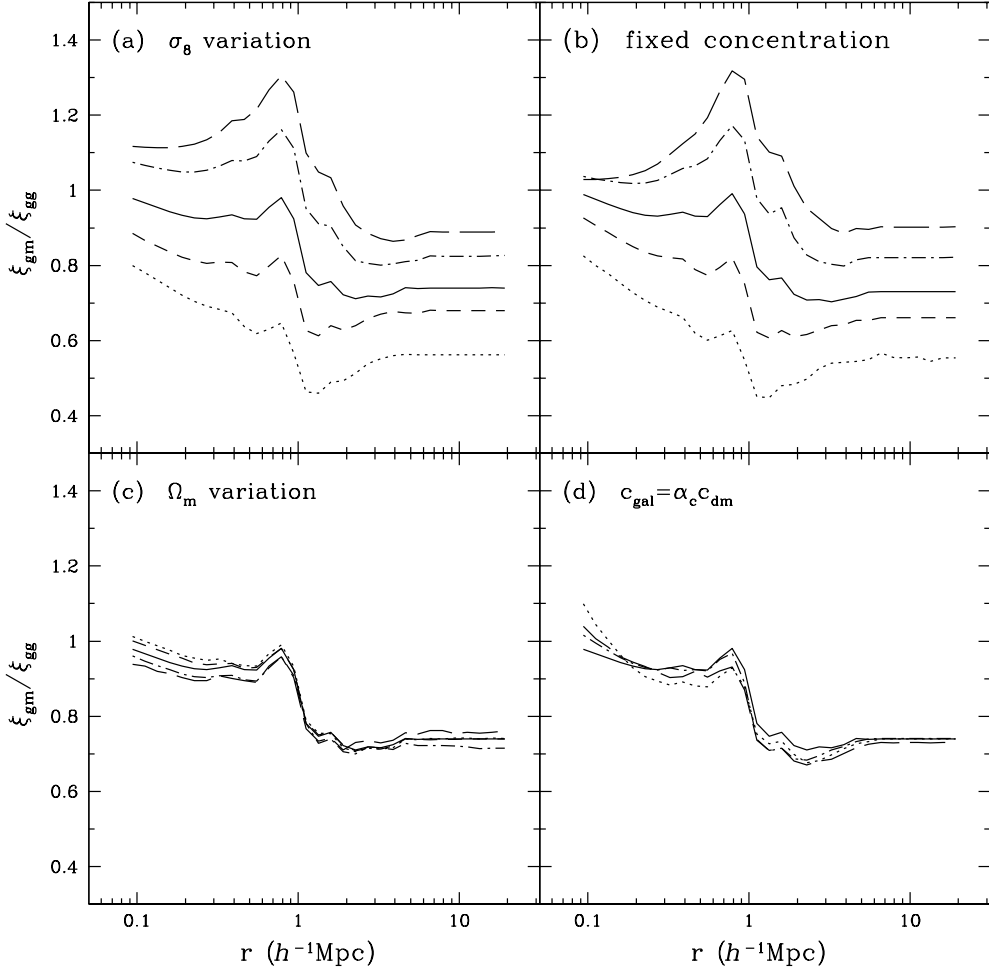
FIG. 9.— The ratio $\xi_{gm}(r)/\xi_{gg}(r)$, which is equal to r_{gm}/b in the linear bias model. Panels (a)-(d) show the four model sequences illustrated in Figs. 7 and 8. Line types follow the same sequence as in those Figures, with σ_8 increasing from 0.6 (*dotted*) to 1.0 (*long-dashed*) in panels (a) and (b), Ω_m increasing from 0.2 (*dotted*) to 0.4 (*long-dashed*) in (c), and α_c increasing from 0.3 (*dotted*) to 1.0 (*solid*) in (d).

Figures 9c and 9d show that the effects of Ω_m or c_{gal} variations are much smaller than those of σ_8 variations. The $\sim 5\%$ model-to-model differences at small scales arise from their different halo concentrations, while the smaller differences at large scales reflect the slight changes in HOD parameters required to match $w_p(r_p)$. Present observations (Hoekstra et al. 2002; Sheldon et al. 2004) are consistent with $\xi_{gm}(r)/\xi_{gg}(r)$ that is approximately scale-independent, but the uncertainties are still fairly large, and testing for the feature predicted in Figure 9 will require more careful replication of observational procedures.

Figure 9 shows that the linear bias expectation of constant $\xi_{gm}(r)/\xi_{gg}(r)$ holds accurately for $r \geq 4\ h^{-1}$Mpc but fails at the 20–50% level in the non-linear regime. We can also ask how well the linear bias prediction $\Delta\Sigma \propto \Omega_m\sigma_8$ describes the *scaling* of $\Delta\Sigma(r)$ with cosmological parameters. To answer this question, and to allow easy scaling of our predictions with cosmological parameters, we adopt the more general formula

$$\frac{\Delta\Sigma(r)}{\Delta\Sigma_{\text{FID}}(r)} = \left(\frac{\Omega_m}{0.3}\right)^{\alpha}\left(\frac{\sigma_8}{0.8}\right)^{\beta} \qquad (17)$$

and determine best-fit values of α and β at each separation

r. Here $\Delta\Sigma_{\text{FID}}(r)$ is the excess surface density prediction of the fiducial model with $\Omega_m = 0.3$ and $\sigma_8 = 0.8$, and we fit α and β using a full grid of models with $\sigma_8 = 0.6, 0.7, 0.8, 0.9, 1.0$ and $\Omega_m = 0.15, 0.2, 0.25, 0.3, 0.35, 0.4, 0.45$. We assume $c_{gal} = c_{dm}$ in all cases.

Figures 10a and 10b plot the fitted values of α and β, respectively, as a function of r. Results for $M_r \leq -20$ galaxies and $M_r \leq -21$ galaxies are similar, though the underlying $\Delta\Sigma_{\text{FID}}(r)$ is different in the two cases. There are two notable departures from the linear bias values $\alpha = \beta = 1$. At small scales, α falls below one, reflecting the weak convergence of $\Delta\Sigma(r)$ curves seen in Figure 8b. This convergence in turn reflects the Ω_m-dependence of halo concentrations. At scales $r \sim 2-5\ h^{-1}$Mpc, β rises above unity, corresponding to the slight divergence of $\Delta\Sigma(r)$ curves at these scales in Figure 7f. Figure 10c shows the rms and maximum fractional errors between the Ω_m or σ_8 dependences predicted by the full analytic model and the scaling relation (17), calculated over our full model grid. The rms errors range from $\sim 1\%$ at large r to $\sim 3\%$ at intermediate r. The largest errors arise for the $\Omega_m = 0.45$, $\sigma_8 = 1.0$ model, and they are roughly twice the rms errors. Figure 10d shows the result of adopting the linear
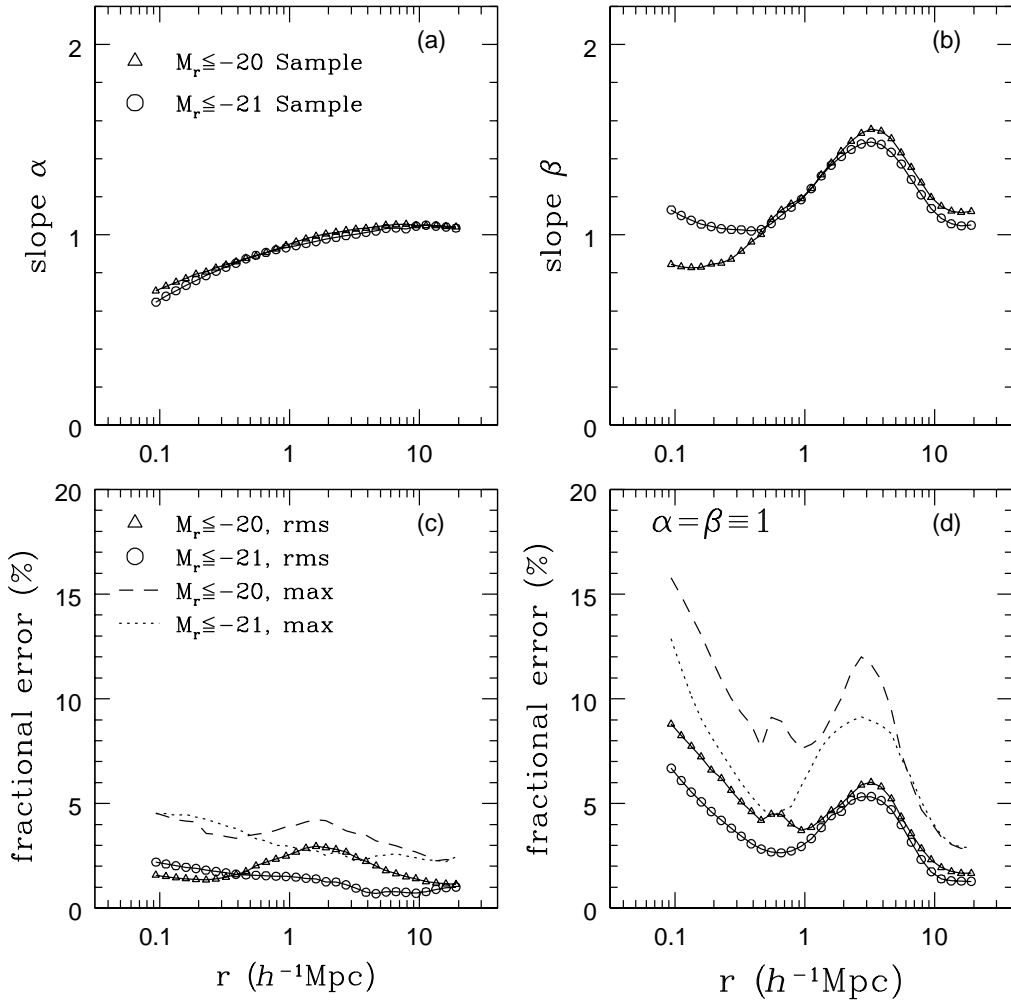
FIG. 10.— Parameters $\alpha(r)$ and $\beta(r)$ of the bias scaling relation $\Delta\Sigma(r) \propto \Omega_m^{\alpha}\sigma_8^{\beta}$ (eq.[17]) for samples matched to the SDSS $w_p(r_p)$ measurements of $M_r \leq -20$ (*triangles*) and $M_r \leq -21$ (*circles*) galaxies. Panel (c) shows the rms and maximum fractional errors of this scaling relation, relative to the full analytic calculation, over a model grid with Ω_m varying from 0.15 to 0.45 and σ_8 varying from $\sigma_8 = 0.6$ to 1.0. Panel (d) shows the same errors for linear bias scaling $\alpha = \beta = 1$. In all cases the maximum error arises for $\Omega_m = 0.45$, $\sigma_8 = 1.0$.

bias scaling $\alpha = \beta = 1$ in equation (17). The linear bias predictions are accurate at the $\sim 1\%$ (rms) to $\sim 3\%$ (maximum error) level for $r \geq 10 \ h^{-1}$Mpc, but the deviations become substantial at smaller r, with errors of $\sim 5-16\%$ at $r = 3 \ h^{-1}$Mpc and $r = 0.1 \ h^{-1}$Mpc for the $\Omega_m = 0.45$, $\sigma_8 = 1.0$ model. The errors of the linear bias scaling are typically a factor $\sim 1.5-4.0$ larger than those using our fitted values of $\alpha(r)$ and $\beta(r)$.

Table 3 lists $\Delta_{\mathrm{FID}}(r)$, the values of $\Delta\Sigma(r)$ predicted by the analytic model for the $M_r \leq -20$ and $M_r \leq -21$ galaxy samples assuming $\Omega_m = 0.3$ and $\sigma_8 = 0.8$. It also lists the $\alpha(r)$ and $\beta(r)$ functions shown in Figure 10. Equation (17) can be used to scale these predictions to other values of Ω_m and σ_8, and measurements of $\Delta\Sigma(r)$ for these galaxy samples could then be used to obtain constraints in the Ω_m-σ_8 plane. Our prediction of $\Delta\Sigma_{\mathrm{FID}}(r)$ is weakly dependent on the HOD parametrization that we adopt when fitting $w_p(r_p)$. If we adopt the alternative parametrization used by Zehavi et al. (2005b), where α_{sat} is fixed to one but the $\langle N_{\mathrm{sat}}\rangle_M$ cutoff is a fit parameter, then the $\Delta\Sigma(r)$ predictions change by less than 5% for all $r > 0.1 \ h^{-1}$Mpc. We have not yet explored more general parametrizations, but we expect that the $\Delta\Sigma(r)$ predictions

would be robust at this level for all HOD models that fit the observed $w_p(r_p)$.

Galaxy-galaxy lensing measurements are often made for flux-limited samples rather than absolute-magnitude limited samples to increase the signal-to-noise ratio, but such measurements are difficult to interpret quantitatively because they do not represent properties of a uniformly defined galaxy population. Because our predictions apply on the non-linear scales where the measurement precision is higher, and because results from different radii can be combined, it should be possible to obtain precise constraints on $\sigma_8\Omega_m$ from absolute magnitude-limited samples, and to use different samples to check for consistency. Since the values of α and β vary with scale, it is possible in principle to break the degeneracy between Ω_m and σ_8. However, the deviations from linear scaling are not large, so while $\sigma_8\Omega_m$ should be well constrained, individual parameter constraints are likely to be imprecise and sensitive to systematic uncertainties in the modeling.

Mandelbaum et al. (2006) have recently presented SDSS measurements for narrow bins of luminosity and of stellar mass, which are well suited to their goal of constraining halo

virial masses and satellite fractions. For cosmological parameter constraints, we think it is better to use luminosity or mass-threshold samples, which provide higher signal-to-noise ratio, and which are easier to model robustly because there is no *upper* mass cutoff on $\langle N_{\text{cen}} \rangle_M$.

6. SUMMARY

We have developed an analytic model to predict $\Delta\Sigma(r)$ for specified cosmological and galaxy HOD parameters and tested its validity using SPH and *N*-body simulations. We have used the analytic model to investigate the dependence of $\Delta\Sigma(r)$ on σ_8 and Ω_m when HOD parameters are chosen to reproduce the observational space density and projected correlation function $w_p(r_p)$ of the galaxy sample being measured. Our main findings are as follows:

1. In our SPH simulation, replacing the satellite galaxies of each halo with randomly selected dark matter particles has a 10–20% effect on $\xi_{\text{gg}}(r)$ and $\xi_{\text{gm}}(r)$ at scales $r \sim 0.5 \ h^{-1}\text{Mpc}$, and smaller impact at other scales. Most of this difference arises from the differing radial profiles of satellite galaxies and dark matter. If satellites are replaced in a way that preserves the radial profile but randomizes azimuthal positions, then changes to $\xi_{\text{gg}}(r)$ and $\xi_{\text{gm}}(r)$ are $\lesssim 10\%$ at all radii, and changes to $\Delta\Sigma(r)$ are $< 5\%$. Dark matter subhalos around individual satellites orbiting in larger halos are present, but they have negligible impact on the global $\Delta\Sigma(r)$.

2. If we randomly reassign the galaxy occupation number of each halo with $M < 4.6 \times 10^{13} \ h^{-1} M_\odot$ to another halo of nearly equal mass, then changes to $\xi_{\text{gg}}(r)$, $\xi_{\text{gm}}(r)$, and $\Delta\Sigma(r)$ are $\lesssim 2\%$ at all $r < 5 \ h^{-1}\text{Mpc}$. This result implies that any environmental dependence of the halo occupation function $P(N|M)$ at fixed halo mass has minimal impact on these statistics for our simulated galaxy sample, which is defined by a baryonic mass threshold. For our largest scale point at $12 \ h^{-1}\text{Mpc}$, we find an effect of 10% on $\xi_{\text{gg}}(r)$, 5% on $\xi_{\text{gm}}(r)$, and 2% on $\Delta\Sigma(r)$, but the statistical uncertainties of our estimate are of comparable magnitude at this scale, so larger simulation volumes are needed to definitively establish the impact of any environmental dependence on the large scale bias factor. Taken together, results 1 and 2 show that the $\xi_{\text{gg}}(r)$ and $\Delta\Sigma(r)$ predictions of a full hydrodynamic simulation can be reproduced to 5% or better (usually much better) by populating the halos of a pure *N*-body simulation with the correct $P(N|M)$, provided that satellite galaxy populations have the correct radial profiles.

3. Our analytic model for $\Delta\Sigma(r)$ is based on the methods introduced by Seljak (2000) and Guzik & Seljak (2001), but it incorporates the scale-dependent halo bias and ellipsoidal halo exclusion corrections introduced by Zheng (2004) and Tinker et al. (2005) for $\xi_{\text{gg}}(r)$ calculations. We have tested the analytic model against numerical results from a grid of populated *N*-body simulations, which span the parameter range $\sigma_8 = 0.6 - 0.95$ and $\Omega_m = 0.1 - 0.63$, with HOD parameters chosen to match the space density and projected correlation function of SDSS galaxy with $M_r \leq -20$ (Zehavi et al. 2005b). The analytic model reproduces the numerical results to 5% or better over the range of $0.1 \ h^{-1}\text{Mpc} \leq r \leq 20 \ h^{-1}\text{Mpc}$. The residuals are consistent with the statistical errors of the numerical calculations, except for the innermost bin, where gravitational force softening in the *N*-body simulations artificially suppresses correlations.

4. For the $M_r \leq -20$ HOD parameters, pairs involving at least one central galaxy dominate the galaxy-galaxy correlation function at $r \lesssim 0.4 \ h^{-1}\text{Mpc}$ and $r \gtrsim 1 \ h^{-1}\text{Mpc}$. In the range $0.4 \ h^{-1}\text{Mpc} \lesssim r \lesssim 1 \ h^{-1}\text{Mpc}$, satellite-satellite pairs in large halos make the dominant contribution to $\xi_{\text{gg}}(r)$. In similar fashion, central galaxies dominate the galaxy-matter correlation function at small and large separations, while satellite galaxies dominate in the range $0.25 \ h^{-1}\text{Mpc} \lesssim r \lesssim 1.5 \ h^{-1}\text{Mpc}$. The halos of individual satellites make negligible contribution to $\Delta\Sigma(r)$ because they are usually tidally truncated below the scales at which the satellite contribution itself is important.

5. For samples with HOD parameters chosen to match the $M_r \leq -21$ SDSS sample of Zehavi et al. (2005b), the ratio $\xi_{\text{gm}}(r)/\xi_{\text{gg}}(r)$ is constant at $r \gtrsim 4 \ h^{-1}\text{Mpc}$, as predicted by the linear bias model, but it jumps by 20–50% at scales $r \sim 1 \ h^{-1}\text{Mpc}$ near the transition from the 1-halo to 2-halo clustering regime, before settling to a new, higher value at small scales. The magnitude of the jump depends on σ_8, and it is likely to depend on the galaxy sample as well, being stronger for more highly clustered populations. In linear bias terms, the large scale values of $\xi_{\text{gm}}(r)/\xi_{\text{gg}}(r)$ correspond to a galaxy-matter cross-correlation coefficient $r_{\text{gm}} \simeq 0.9$, if we define the bias factor $b = [\xi_{\text{gg}}(r)/\xi_{\text{mm}}(r)]^{1/2}$.

6. We fit the dependence of $\Delta\Sigma(r)$ on cosmological parameters with a scaling formula $\Delta\Sigma(r) \propto \Omega_m^\alpha \sigma_8^\beta$, where α and β are slowly varying functions of r. This scaling describes the results of our full analytic model with rms error $\lesssim 3\%$ over the parameter range $\Omega_m = 0.15 - 0.45$, $\sigma_8 = 0.6 - 1.0$. At large scales, α and β approach the linear bias values $\alpha = \beta = 1$. However, forcing $\alpha = \beta = 1$ at all scales leads to errors that are larger by factors of $1.5 - 4.0$, relative to the scaling formula (17) with our fitted values of α and β.

Table 3 lists our predicted values of $\Delta\Sigma(r)$ for the $M_r \leq -20$ and $M_r \leq -21$ SDSS samples, assuming our fiducial cosmological model with $\Omega_m = 0.3$ and $\sigma_8 = 0.8$. Equation (17) allows scaling of these results to other values of σ_8 and Ω_m, and measurements of $\Delta\Sigma(r)$ for these samples can be combined with these predictions to obtain cosmological constraints, which will be tightest on a parameter combination that is approximately $\sigma_8 \Omega_m$. Given the growth of the SDSS since the samples analyzed by Sheldon et al. (2004) and Zehavi et al. (2005b), it is probably preferable to extract $w_p(r_p)$ and $\Delta\Sigma(r)$ estimates for matched galaxy samples from the latest data sets. A full analysis should also investigate the effects of adding greater flexibility to the HOD parametrization itself, using, e.g., the 5-parameter formulation of Zheng et al. (2005). We have tested the effect of changing to a different 3-parameter description (see § 5), and we find changes of $\lesssim 5\%$ in the $\Delta\Sigma(r)$ predictions. We suspect that these predictions would remain similar for any choice of HOD parameters that reproduces the observed $w_p(r_p)$. Our SPH and *N*-body tests indicate that the analytic model predictions should be accurate to 5% or better given our HOD parametrization, though assumptions about galaxy profile concentrations have significant effect at $r < 2 \ h^{-1}\text{Mpc}$. This level of accuracy is adequate given the statistical errors expected for current samples, but refinement and testing on large simulations will be needed to take full advantage of future analyses of even larger, deeper surveys. Precise determinations of Ω_m and σ_8 can play an important role in testing theories of dark energy and models of inflation, making galaxy-galaxy lensing an essential element of observational cosmology.

REFERENCES

Abazajian, K., et al. 2005, ApJ, 625, 613
Benson, A. J., Baugh, C. M., Cole, S., Frenk, C. S., & Lacey, C. G. 2000, MNRAS, 316, 107
Berlind, A. A., & Weinberg, D. H. 2002, ApJ, 575, 587
Berlind, A. A., et al. 2003, ApJ, 593, 1
Blandford, R. D., Saust, A. B., Brainerd, T. G., & Villumsen, J. V. 1991, MNRAS, 251, 600
Blanton, M. R., et al. 2003, ApJ, 592, 819
Blanton, M. R., Eisenstein, D. J., Hogg, D. W., & Zehavi, I. 2006, ApJ, in press (astro-ph/0411037)
Bond, J. R., Cole, S., Efstathiou, G., & Kaiser, N. 1991, ApJ, 379, 440
Brainerd, T. G., Blandford, R. D., & Smail, I. 1996, ApJ, 466, 623
Bryan, G. L., & Norman, M. L. 1998, ApJ, 495, 80
Bullock, J. S., et al. 2001, MNRAS, 321, 559
Bullock, J. S., Wechsler, R. H., & Somerville, R. S. 2002, MNRAS, 329, 246
Cole, S., et al. 2005, MNRAS, 362, 505
Collister, A. A., & Lahav, O. 2005, MNRAS, 361, 415
Cooray, A., & Sheth, R. 2002, Phys. Rept., 372, 1
Croton, D. J., et al. 2006, MNRAS, 365, 11
Croton, D. J., Gao, L., White, S. D. M. 2006, MNRAS, submitted (astro-ph/0605636)
Davé, R., Dubinski, J., & Hernquist, L. 1997, NewA, 2, 277
Davis, M., Efstathiou, G., Frenk, C. S., & White, S. D. M. 1985, ApJ, 292, 371
Dekel, A., & Lahav, O. 1999, ApJ, 520, 24
Efstathiou, G., Bond, J. R., & White, S. D. M. 1992, MNRAS, 258, 1
Evrard, A. E., Summers, F. J., & Davis, M. 1994, ApJ, 422, 11
Fischer, P., et al. 2000, AJ, 120, 1198
Gao, L., Springel, V., & White, S. D. M. 2005, MNRAS, 363, L66
Gladders, M. D., & Yee, H. K. C. 2001, in ASP Conf. Ser. 232, The New Era of Wide Field Astronomy, ed. R. Clowes, A. Adamson, & G. Bromage (San Francisco: ASP)
Guzik, J., & Seljak, U. 2001, MNRAS, 321, 439
Guzik, J., & Seljak, U. 2002, MNRAS, 335, 311
Harker, G., Cole, S., Helly, J., Frenk, C., & Jenkins, A. 2006, MNRAS, 367, 1039
Hernquist, L., & Katz, N. 1989, ApJS, 70, 419
Hoekstra, H., Yee, H. K. C., & Gladders, M. D. 2001, ApJ, 558, 11L
Hoekstra, H., van Waerbeke, L., Gladders, M. D., Mellier, Y., & Yee, H. K. C. 2002, ApJ, 577, 604
Jenkins, A., Frenk, C. S., White, S. D. M., Colberg, J. M., Cole, S., Evard, A. E., Couchman, H. M. P., & Yoshida, N. 2001, MNRAS, 321, 372
Johnston, D. E., Sheldon, E. S., Tasitsiomi, A., Frieman, J. A., Wechsler, R., & McKay, T. A. 2005, ApJ, submitted (astro-ph/0507467)
Jing, Y. P., Mo, H. J., & Börner, G. 1998, ApJ, 503, 37
Jing, Y. P., Börner, G., & Suto, Y. 2002, ApJ, 564, 15
Kaiser, N. 1984, ApJ, 284, L9
Kaiser, N. 1987, ApJ, 227, 1
Kaiser, N. 1992, ApJ, 388, 272
Katz, N., Hernquist, L., & Weinberg, D. H. 1992, ApJ, 399, 109L
Katz, N., Weinberg, D. H., & Hernquist, L. 1996, ApJS, 105, 19
Kauffmann, G., Nusser, A., & Steinmetz, M. 1997, MNRAS, 286, 795
Kochanek, C. S., & White, M. 2001, ApJ, 559, 531
Kravtsov, A. V., Berlind, A. A., Wechsler, R. H., Klypin, A. A., Gottlöber, S., Allgood, B., & Primack, J. R. 2004, ApJ, 509, 35
Lee, K.-S., Mauro, G., Gnedin, O. Y., Somerville, R., Ferguson, H., Dickinson, M., & Ouchi, M. 2006, ApJ, 642, 63
Lemson, G., & Kauffmann, G. 1999, MNRAS, 302, 111
Ma, C.-P., & Fry, J. N. 2000, ApJ, 543, 503
Mandelbaum, R., Tasitsiomi, A., Seljak, U., Kravtsov, A. V., & Wechsler, R. H. 2005, MNRAS, 362, 1451

Mandelbaum, R., Seljak, U., Kauffmann, G., Hirata, C. M., & Brinkmann, J. 2006, MNRAS, 368, 715
Magliocchetti, M., & Porciani, C. 2003, MNRAS, 346, 186
McKay, T. A., et al. 2001, astro-ph/0108013
Miralda-Escudé, J. 1991a, ApJ, 370, 1
Miralda-Escudé, J. 1991b, ApJ, 380, 1
Mo, H. J., & White, S. D. M. 1996, MNRAS, 282, 1096
Nagai, D., & Kravtsov, A. V. 2005, ApJ, 618, 557
Natarajan, P., Kneib, J.-P., & Smail, I. 2002, ApJ, 580, L11
Navarro, J. F., Frenk, C. S., & White, S. D. M. 1997, ApJ, 490, 493
Peacock, J. A., & Smith, R. E. 2000, MNRAS, 318, 1144
Pen, U. 1998, ApJ, 504, 601
Porciani, C., Magliocchetti, M., & Norberg, P. 2004, MNRAS, 355, 1010
Press, W. H., & Schechter, P. 1974, ApJ, 187, 425
Scherrer, R. J., & Bertschinger, E. 1991, ApJ, 381, 349
Scoccimarro, R., Sheth, R. K., Hui, L., & Jain, B. 2001, ApJ, 546, 20
Seljak, U. 2000, MNRAS, 318, 203
Seljak, U. 2001, MNRAS, 325, 1359
Seljak, U., & Warren, M. S. 2004, MNRAS, 355, 129
Seljak, U., & Zaldarriaga, M. 1996, ApJ, 469, 437
Seljak, U., et al. 2005, PRD, 71, 103515
Sheldon, E. S., et al. 2004, AJ, 127, 2544
Sheth, R. K., Hui, L., Diaferio, A., & Sccoccimarro, R. 2001a, MNRAS, 325, 1288
Sheth, R. K., Mo, H. J., & Tormen, G. 2001b, MNRAS, 323,1
Sheth, R. K., & Tormen, G. 1999, MNRAS, 308, 119
Sheth, R. K., & Tormen, G. 2002, MNRAS, 329, 61
Sheth, R. K., & Tormen, G. 2004, MNRAS, 350, 1385
Smith, R. E., et al. 2003, MNRAS, 341, 1311
Spergel, D. N., et al. 2003, ApJS, 148, 175
Springel, V., Yoshida, N., & White, S. D. M. 2001, NewA, 6, 79
Tasitsiomi, A., Kravtsov, A. V., Wechsler, R. H., Primack, J. P. 2004, ApJ, 614, 533
Tegmark, M., et al. 2004, ApJ, 606, 702
Tinker, J. L., Weinberg, D. H., Zheng, Z., & Zehavi, I. 2005, ApJ, 631, 41
Tinker, J. L., Weinberg, D. H., & Zheng, Z. 2006, MNRAS, 368, 85
Weinberg, D. H., Colombi, S., Davé, R., & Katz, N. 2006, ApJ, submitted (astro-ph/0604393)
Weinberg, D. H., Davé, R., Katz, N., & Hernquist, L. 2004, ApJ, 601, 1
White, M. 2001, MNRAS, 321, 1
White, S. D. M. 1996, in Proceedings of the Les Houches Summer School, ed. by R. Schaeffer, J. Silk, M. Spiro, & J. Zinn-Justin. 1996, p.349
White, S. D. M., Efstathiou, G., Frenk, C. S. 1993, MNRAS, 262, 1023
White, S. D. M., Hernquist, L., & Springel, V. 2001, MNRAS, 550, 129
Yang, X. H., Mo, H. J., & van den Bosch, F. C. 2003, MNRAS, 339, 1057
York, D., et al. 2000, AJ, 120, 1579
Yoshikawa, K., Taruya, A., Jing, Y. P., & Suto, Y 2001, ApJ, 558, 520
Zehavi, I., et al. 2002, ApJ, 571, 172
Zehavi, I., et al. 2004, ApJ, 608, 16
Zehavi, I., et al. 2005a, ApJ, 621, 22
Zehavi, I., et al. 2005b, ApJ, 630, 1
Zentner, A. R., Berlind, A. A., Bullock, J. S., Kravtsov, A. V., & Wechsler, R. H. 2005, ApJ, 624, 505
Zheng, Z., Tinker, J. L., Weinberg, D. H., & Berlind, A. A. 2002, ApJ, 575, 617
Zheng, Z. 2004, ApJ, 610, 61
Zheng, Z., et al. 2005, ApJ, 633, 791